Draft version May 4, 2026
Typeset using LaTeX **twocolumn** style in AASTeX7.0.1

arXiv:2605.00822v1 [astro-ph.GA] 1 May 2026

# PEARLS: Two Distinct Populations of AGN Hosts Moving Between Star Formation and Quiescence

Gibson B. Bowling [1], Rafael Ortiz III [1], S. P. Willner [2], Seth H. Cohen [1], Timothy Carleton [1], Rogier A. Windhorst [1], Rolf A. Jansen [1], Christopher N. A. Willmer [3], W. Peter Maksym [4], Anton M. Koekemoer [5], Madeline A. Marshall [6], Rosalia O'Brien [7,1], Payaswini Saikia [8], Massimo Ricotti [9], Jordan C. J. D'Silva [10,11], Dan Coe [5,12,13], Christopher J. Conselice [14], Jose M. Diego [15], Simon P. Driver [10], Brenda L. Frye [16], Norman A. Grogin [5], Rachel Honor [1], Jake Summers [17,18], Nor Pirzkal [5], Aaron Robotham [10], Russell E. Ryan, Jr. [5], Brent M. Smith [1], Haojing Yan [19], Cheng Cheng [20,21], Liam Nolan [22], Heidi B. Hammel [23], and Stefanie N. Milam [24]

[1] *School of Earth and Space Exploration, Arizona State University, Tempe, AZ 85287-1404, USA*
[2] *Center for Astrophysics | Harvard & Smithsonian, 60 Garden Street, Cambridge, MA, 02138, USA*
[3] *Steward Observatory, University of Arizona, 933 N Cherry Ave, Tucson, AZ, 85721-0009, USA*
[4] *NASA Marshall Space Flight Center, Huntsville, AL 35812, USA*
[5] *Space Telescope Science Institute, 3700 San Martin Drive, Baltimore, MD 21218, USA*
[6] *Los Alamos National Laboratory, Los Alamos, NM 87545, USA*
[7] *University of Maryland/CRESST2, NASA Goddard Space Flight Center, Greenbelt, MD 20771, USA*
[8] *Department of Astronomy, Yale University, PO Box 208101, New Haven, CT 06520-8101, USA*
[9] *Dept. of Astronomy, University of Maryland, College Park, MD 20742, USA*
[10] *International Centre for Radio Astronomy Research (ICRAR) and the International Space Centre (ISC), The University of Western Australia, M468, 35 Stirling Highway, Crawley, WA 6009, Australia*
[11] *ARC Centre of Excellence for All Sky Astrophysics in 3 Dimensions (ASTRO 3D), Australia*
[12] *Association of Universities for Research in Astronomy (AURA) for the European Space Agency (ESA), STScI, Baltimore, MD 21218, USA*
[13] *Center for Astrophysical Sciences, Department of Physics and Astronomy, The Johns Hopkins University, 3400 N Charles St. Baltimore, MD 21218, USA*
[14] *Jodrell Bank Centre for Astrophysics, Alan Turing Building, University of Manchester, Oxford Road, Manchester M13 9PL, UK*
[15] *Instituto de Física de Cantabria (CSIC-UC). Avenida. Los Castros s/n. 39005 Santander, Spain*
[16] *Department of Astronomy/Steward Observatory, University of Arizona, 933 N Cherry Ave, Tucson, AZ, 85721-0009, USA*
[17] *TAPIR, California Institute of Technology, Pasadena, CA 91125, USA*
[18] *LIGO Laboratory, California Institute of Technology, Pasadena, CA 91125, USA*
[19] *Department of Physics and Astronomy, University of Missouri, Columbia, MO 65211, USA*
[20] *Chinese Academy of Sciences South America Center for Astronomy, National Astronomical Observatories, CAS, Beijing 100101, China*
[21] *Key Laboratory of Optical Astronomy, NAOC, 20A Datun Road, Chaoyang District, Beijing 100101, China*
[22] *Department of Astronomy, University of Illinois at Urbana-Champaign, Urbana, IL 61801, USA*
[23] *Association of Universities for Research in Astronomy, 1331 Pennsylvania Avenue NW, Suite 1475, Washington, DC 20005, USA*
[24] *NASA Goddard Space Flight Center, Greenbelt, MD 20771, USA*

## ABSTRACT

We present the results of AGN–host-galaxy decomposition using JWST/NIRCam, HST/ACS, and HST/WFC3 imaging of the North Ecliptic Pole Time Domain Field (NEP-TDF). The light-profiles of 36 NIRCam-selected AGN candidates are modeled for measurement of their point sources, and point source-subtracted host-galaxy emission is used in SED modeling for star formation rate (SFR) estimation. Offsets from the canonical star-forming main sequence (SFMS) show that the host galaxies form two distinct groups distinguished by their star formation: a "bridge" between the moderate SFRs of radio sources and low SFRs of X-ray sources, and a cleanly-separated "branch" above $\Delta\mathrm{SFMS} = -1$ whose SFR trends positively with AGN fraction. Branch galaxies include late-type galaxies with X-ray and radio detections and more dominant point sources that are most certainly AGN, while bridge galaxies have predominantly early-type morphologies with weaker point sources that may be due to compact stellar bulges. Both groups show evidence of recent transition between star formation and

Corresponding author: Gibson B. Bowling
gbbowlin@asu.edu

quiescence, but neither group shows preference for higher or lower stellar mass or redshift, suggesting that star formation in NIRCam-selected AGN-hosts is more strongly determined by AGN activity than by stellar mass.

*Keywords:* AGN host galaxies (2017) — Galaxies (573) — Star formation (1569) — Spectral energy distribution (2129) — James Webb Space Telescope (2291) — Hubble Space Telescope (761)

## 1. INTRODUCTION

The centers of most galaxies harbor supermassive black holes (SMBHs; e.g., J. Kormendy & D. Richstone 1995; J. Magorrian et al. 1998; D. Richstone et al. 1998), and their distinct signatures give rise to observations unique to the nuclear regions of galaxies (e.g., C. K. Seyfert 1943; G. Burbidge 1970; E. Y. Khachikian & D. W. Weedman 1974; T. M. Heckman 1980; H. D. Tran 1995a,b,c). Accreting SMBHs are the central engines of active galactic nuclei (AGN) that radiate across the entirety of the electromagnetic spectrum (e.g., C. K. Seyfert 1943; B. L. Fanaroff & J. M. Riley 1974; M. Elvis et al. 1978; D. Stern et al. 2005). One observational signature of many AGN is a nuclear point source (e.g., M. Schmidt 1963; C. Hazard et al. 1963; J. K. Kotilainen et al. 1992a,b; E. A. Ramírez et al. 2014; R. Giacconi et al. 2001; J. S. Dunlop et al. 2003; D. M. Alexander et al. 2003; M. Lacy et al. 2004; N. L. Zakamska et al. 2006; S. Gezari et al. 2013; R. Ortiz et al. 2024; P. Saikia et al. 2025) that appears as the telescope aperture's point spread function (PSF) superimposed on the host-galaxy light profile.

The interactions of AGN and their host galaxies are complex and represent a critical phase in the evolution of massive galaxies (e.g., G. Kauffmann et al. 2003; L. J. Kewley et al. 2006). AGN are known both to suppress (quench; e.g., J. Silk & M. J. Rees 1998; A. C. Fabian 1999; E. Sturm et al. 2011; A. C. Fabian 2012; S. Laha et al. 2021) and enhance (e.g., W. van Breugel et al. 2004; P.-C. Zinn et al. 2013; S. Nayakshin 2014; A. Kirkpatrick et al. 2020; M.-Y. Zhuang et al. 2021; P. Joseph et al. 2022; K. J. Duncan et al. 2023) the star-formation rates (SFRs) of their host galaxies in negative or positive feedback processes, respectively.

The star formation in galaxies is strongly dependent on mass and redshift (e.g., P. Madau & M. Dickinson 2014; L. Bisigello et al. 2018), and so it is useful to contextualize SFRs with respect to a canonical star-forming main sequence (SFMS; K. G. Noeske et al. 2007) relating the SFR to stellar mass and redshift calibrated by observations of many star-forming galaxies (e.g., J. S. Speagle et al. 2014; P. Popesso et al. 2023). The result is a 4-tiered classification scheme for galaxies that includes (1) nominal star formation consistent with the SFMS, (2) starburst (enhanced star formation significantly above the SFMS), (3) transitional (star formation that is below the SFMS and that may be "ramping down"), and (4) quiescence, which is characterized by star formation significantly below the SFMS or not detectable. In the context of AGN-host studies, quiescence may be taken to mean quenched, though they are not always synonymous. Observationally calibrated models predict that starburst galaxies smoothly become post-starburst galaxies with rapidly decreasing SFR (e.g., K. E. Whitaker et al. 2012; S. G. Patel et al. 2012; L. Wang et al. 2019), eventually becoming quiescent. Galaxies are not confined to a single phase during their lifetimes, and this is in part due to AGN.

Historically, photometric classification of IR-bright galaxies has been subject to degeneracy due to the detection bias at IR wavelengths: stars and dust-obscured AGN both shine bright in the NIR (e.g., A. Sajina et al. 2005), and correlation between IR luminosity and starburst activity is common (e.g., D. Farrah et al. 2003; M. Blank & W. J. Duschl 2012). Corrections to AGN selection schemes (e.g., J. L. Donley et al. 2012) and spectral-energy distribution (SED)-fitting routines (e.g., M. Stalevski 2012; M. Stalevski et al. 2016) have been developed to address this, but they have been forced by limited angular resolution to use the combined AGN+host emission to derive an AGN fraction and galaxy properties rather than deriving host-galaxy properties from galaxy emission alone. This makes the fits subject to systematic biases, especially in the NIR and at high redshifts, where the spatial and spectroscopic resolutions have been most limited (e.g., G. Roberts-Borsani et al. 2021), even with flagship observatories (e.g., G. G. Fazio et al. 2004).

Since becoming operational in 2022, JWST's NIRCam has brought next-generation sensitivity and resolution to the NIR (J. P. Gardner et al. 2023; M. J. Rieke et al. 2023). NIRCam is uniquely suited to resolve the host galaxies of IR-bright AGN and probe their star-forming properties. Recent studies using the James Webb Space Telescope (JWST) have shown that morphological selection of AGN on the basis of a central point-source is

successful, as demonstrated based on candidates' colors (e.g., D. Stern et al. 2012; R. J. Assef et al. 2013) and by AGN fraction determined from the spectral-energy distribution (e.g., R. Ortiz et al. 2024). Additional confirmation has come from 3 GHz VLA observations (S. P. Willner et al. 2023, 2026) and from VLBA detections (P. Saikia et al. 2025). There is no single way to detect all AGN without extensive multi-wavelength coverage, and the infrared offers a critical vantage point in the search for less-luminous AGN that are undetected in the UV–visible (e.g., D. D. Kocevski et al. 2023; G. Yang et al. 2023; J. Lyu et al. 2024; M. A. Latif et al. 2024; G. H. Rieke et al. 2025; N. Bonaventura et al. 2026).

This study considers the host galaxies of 36 NIRCam-selected AGN candidates and compares their star-forming properties to those of X-ray- and radio-selected AGN. The paper is organized as follows. Section 2 discusses the data used in this study and the construction of a sample of NIRCam-selected AGN candidates. Section 3 describes the light-profile fitting of the sample and measurement of point sources. Section 4 describes the SED fitting and its results and discusses the star-forming properties of the sample with respect to X-ray- and radio-selected samples. A summary of the results and discussion of future prospects is in Section 5. All magnitudes are presented in AB units (J. B. Oke & J. E. Gunn 1983), and, where necessary, we assume a flat ΛCDM cosmology with $H_0 = 68$ km s$^{-1}$ Mpc$^{-1}$, $\Omega_{\rm matter} = 0.32$, and $T_{\rm CMB} = 2.725$ ( Planck Collaboration et al. 2016, 2020).

## 2. DATA & SAMPLE SELECTION

### 2.1. *Observations*

In a previous study, R. Ortiz et al. (2024, O24 henceforth) identified AGN candidates in the JWST North Ecliptic Pole Time Domain Field (NEP-TDF: RA, Decl. = 17:22:47.9, +65:49:22 J2000, ∼15′ diameter; R. A. Jansen & R. A. Windhorst 2018.) JWST/NIRCam images of the NEP-TDF in the F090W, F115W, F150W, F200W, F277W, F356W, F410M, and F444W filters from the Prime Extragalactic Areas for Reionization and Lensing Science (PEARLS) GTO program (P.I.: R. A. Windhorst, PID 2738 R. A. Windhorst et al. 2023) were used. Images were first processed using the STScI `CALWEBB` pipeline for basic data reduction. A customized sky-subtraction and image combination routine (described by R. A. Windhorst et al. 2023) was then used to generate final mosaics with pixel scales of 0.″030 pixel$^{-1}$ and alignment to a GAIA DR3[25] absolute astrometric grid. The 5$\sigma$ point-source depth extends down to ∼29.5 mag (R. A. Windhorst et al. 2023). O24 gives further details of observations and reduction.

Images of the NEP-TDF using the Hubble Space Telescope (HST) Wide Field Camera 3 UVIS channel (WFC3/UVIS) F275W filter and the Advanced Camera for Surveys Wide Field Camera (ACS/WFC) F435W and F606W filters provide additional rest-frame UV–visible constraints on the sample galaxies' star formation. The images were constructed with 0.″030 pixel$^{-1}$ pixel scales and are the data products of HST GO 15278 (P.I.: R. A. Jansen) and the HST TREASURE-HUNT program (GO 16252+16793; PIs: R. A. Jansen & N. A. Grogin) with 2$\sigma$ limiting magnitudes down to ∼29.5 mag. R. O'Brien et al. (2024) and R. A. Jansen et al. (in prep.) give further details regarding observations and reduction.

For measurements of galaxy-integrated flux in JWST and HST bands, the photometry provided by the O24 catalog was used. Where available, spectroscopic redshifts from the MMT Observatory's Binospec and Hectospec instruments (X. Zhao et al. 2024; R. Silver et al. 2026, and C. N. A. Willmer et al., in prep.) were used. For objects without spectroscopic redshifts, the photometric redshifts from O24 were used instead.

### 2.2. *AGN- & QSO-like Object Selection*

Objects were selected from the O24 central point-source galaxy (CPG) catalog. The catalog includes both a core type classification (point source, bulge, or undetermined) based on morphology and an AGN emission fraction $f_{\rm AGN}$ measured over $0.1 - 30.0$ $\mu$m derived from fitted SEDs. For this work, objects with point-source cores or with $f_{\rm AGN} \geq 0.3$ were selected. A point-source core was not used as the sole selection criterion because of the uncertainty in the O24 morphological classification (e.g., ID 48, considered for this study, is classified as a bulge, but has X-ray and radio counterparts, and a central point-source in NIRCam imaging). Central point-source features indicate a highly luminous and compact nuclear region suggestive of an AGN, while $f_{\rm AGN} \geq 0.3$ additionally suggests a substantial AGN component to the SED, which is useful especially in cases where mid-IR or sub-millimeter photometry are not available (e.g., L. Ciesla et al. 2015). Near-infrared (NIR) colors were not considered in the selection because some objects in the O24 catalog are not classified as AGN by their colors despite having point-source cores (O24, their Figure 9) and/or $f_{\rm AGN} \geq 0.3$ (e.g., ID 63, which is considered in this study).

[25] https://www.cosmos.esa.int/web/gaia/dr3

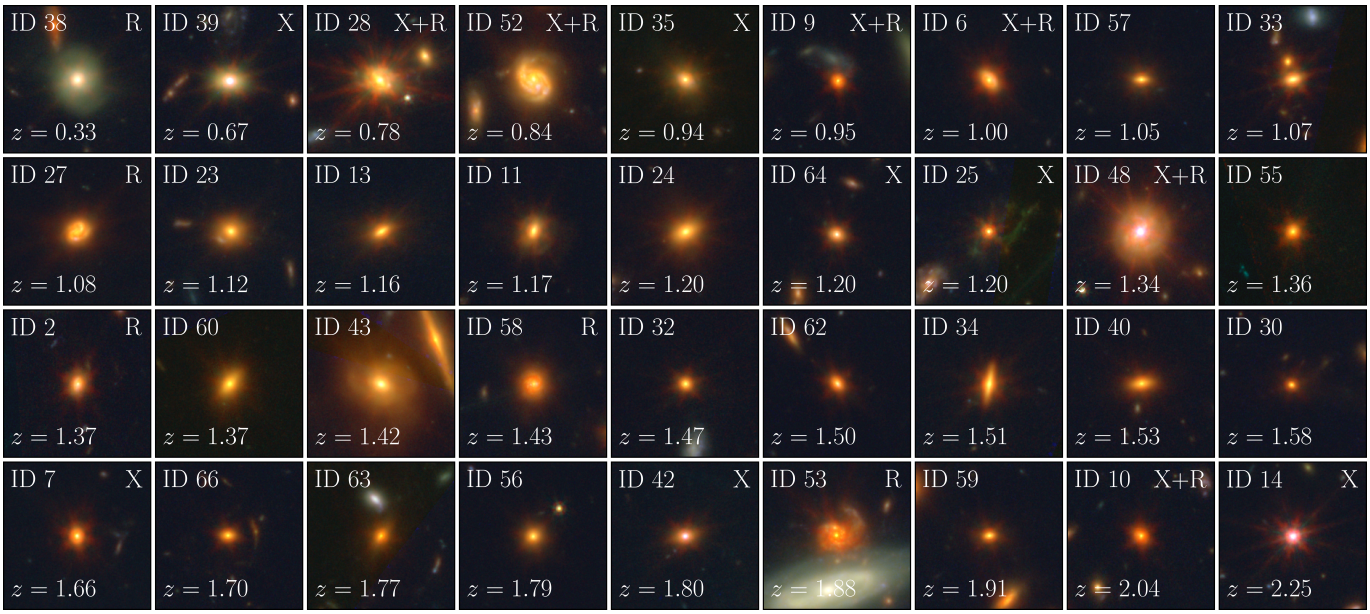



**Figure 1.** RGB image cutouts of the sample galaxies. Stamps are shown in order of increasing redshift and are ∼6″ on a side. Each object's redshift and O24 ID are shown in the lower and upper left corners of their stamps, respectively. Objects with X-ray counterparts have an X in the top right corner, objects with radio counterparts have an R, and objects with both have X+R. The image RGB colors use the `Trilogy`[a] (D. Coe et al. 2012) prescription from the 11 filters of HST+JWST coverage. The color channels are R = F444W+F410M+F356W, G = F277W+F200W+F150W, and B = F115W+F090W+F606W+F435W+F275W.

[a] https://github.com/dancoe/Trilogy

The above criteria select 36/66 CPGs from the O24 catalog.[26]

The sample is morphologically diverse, as shown in Figure 1. It contains both early- (e.g., IDs 39 and 60) and late-type (e.g., IDs 27 and 53) galaxies. Several objects have resolved structure in their hosts (e.g., off-center UV–visible clumps in ID 52 or apparent flocculent and anemic spiral structure in IDs 58 and 48, respectively), though the structures of most of the hosts are outshone by the central point sources.

### 2.3. *Comparative X-Ray and Radio Samples*

To identify X-ray counterparts to sample galaxies, we used the X-ray catalog from W. P. Maksym et al. (in prep.), which is compiled from Chandra X-ray Observatory (CXO) ACIS-I and ACIS-S observations of the entire field over a net 1.8 Ms exposure time. To identify radio counterparts, we used the M. Hyun et al. (2023) 3 GHz catalog with $1\sigma$ noise of $\sim$1 $\mu$Jy beam$^{-1}$ based on observations with the NSF's Karl G. Jansky Very Large Array (VLA).[27]

For comparison of NIRCam-selected sample's star-forming properties to the star-forming properties of X-ray-selected AGN in the field, we used the R. Ortiz et al. (2026, in prep.) catalog of SED parameters of X-ray sources as seen by X. Zhao et al. (2024) and R. Silver et al. (2026). This catalog is the result of extensive multi-wavelength analysis combining NuSTAR and XMM-Newton X-ray fluxes with GALEX (D. C. Martin et al. 2005), SDSS (D. G. York et al. 2000), DECaLS (A. Dey et al. 2019), MMT/MMIRS (C. N. A. Willmer et al. 2023), Subaru/HSC (S. Miyazaki et al. 2018), WISE (E. F. Schlafly et al. 2019), HST, and JWST photometry. Objects in this catalog are required to have 4 broadband detections. To prevent comparison with ill-constrained SED results, only objects whose SED had $\chi^2_\nu \leq 10$ are considered in this study. Within this quality cut, we considered only objects with $f_{\rm AGN} \geq 0.3$ to ensure that that the X-ray-selected sample was comparable to the NIRCam-selected sample.

[26] The F444W fit failed for O24 ID 1 because the image core was saturated in this filter. A similar fit in F277W (S. P. Willner et al. 2026) succeeded in finding a point-source core. This object is nevertheless excluded from our sample because saturation in the three longest-wavelength filters prevents reliable host-galaxy photometry, necessary for the analysis in this work.

[27] The National Radio Astronomy Observatory is a facility of the National Science Foundation operated under cooperative agreement by Associated Universities, Inc.

For similar comparisons to radio-selected objects, we used the S. P. Willner et al. (2026) catalog of SED parameters of NIRCam counterparts to radio detections in the field. The physical properties were derived from UV–NIR photometry from HST and JWST in combination with VLA 3 GHz fluxes. Only objects with $f_{\rm AGN} \geq 0.3$ were selected from this catalog so that the radio-selected sample was comparable to the NIRCam-selected sample.

After cross-matching X-ray and radio detections, 13/36 objects have X-ray counterparts and 11/36 objects have radio counterparts, with 6/36 having both. The sample is tabulated in Table 1, where the core type and $f_{\rm AGN}$ from O24 are listed for reference alongside the X-ray and/or radio counterpart ID(s) if applicable.

## 3. MEASUREMENT OF NUCLEAR POINT SOURCES

### 3.1. *Light-Profile Modeling*

A crucial element of morphological AGN selection is distinguishing nuclear point sources from bright, compact bulges that may appear with point-source features. For galaxies in the NEP-TDF, O24 fit model light profiles using only the JWST/F444W images rather than the full suite of available HST+JWST filters, and point-source presence was determined only on the basis of best-fit $\chi^2_\nu$ comparison. For the purposes of O24, the $\chi^2_\nu$ treatment was sufficient, but using all available broadband imaging best treats the wavelength dependence of the AGN emission within the host galaxy.

For this work, three-component model light profiles were fit to the sample in all filters with detections in the O24 catalog. This was done using `GALFIT` version 3.0.5 (C. Y. Peng et al. 2002, 2010). The model components included one point source and two Sérsic (J. L. Sérsic 1963) profiles, conceptually representing a compact bulge and a more extended disk but with a wide range of free parameters. The intention was not a complete representation of the galaxy's structural parameters but only a measurement of the galaxy's central flux to allow an accurate measurement of the central point-source magnitude. The technical `GALFIT` prescription is in Appendices A and B. The `GALFIT` parameter space was left free enough to iterate towards a physically sensible best-fit solution, and a point-source magnitude was always recovered, even when its flux was negligible compared to the host galaxy. Results of the 11-filter fitting procedure for three objects are shown in Figure 2. The best-fit parameters for the JWST filters are listed in Table 2.

Figure 2 shows a smooth increase in the point-source brightness between filters, going from nearly invisible in the HST and short-wavelength NIRCam filters to dominant in the redder NIRCam filters. Using a three-component model for all galaxy images means that differences between types of models cannot produce spurious results concerning the *presence* of a point source. This is especially important for "model continuity" purposes, where, e.g., if a point source is present in a JWST/F277W image, one would expect it also to be present in the corresponding JWST/F356W and redder images. This was achieved in the fitting results.

Occasionally, "leftover" flux can be seen in the JWST filter residuals. In many cases, the residual structures appear to be from non-axisymmetric features of the host galaxies (e.g., clumps, spiral structure, dust lanes, etc.) that cannot be accounted for using a strictly Sérsic-based model. Direct measurement of these features from the residuals with `SourceExtractor` using the same configuration as O24[28] showed that their mean magnitudes were in the range of ∼27–29 mag in F444W, which is magnitudes fainter than the disk or bulge components found by `GALFIT` (see Table 2) and is therefore not problematic *for measuring point-source magnitudes*.

### 3.2. *Uncertainty in the Point-Source Magnitude*

The purpose of modeling a galaxy's light profile is to gain some insight into what its "true" light profile may be. However, model light profiles can never be taken to be perfect, and the "true" light profile of a galaxy can never be known exactly. In this study, `GALFIT` is capable of fitting light profiles so that $\chi^2_\nu \sim 1$ (see §2.2 of C. Y. Peng et al. 2002), but this can never be taken as an indicator of a truly perfect fit because the data are never perfectly reproduced by models. As such, `GALFIT`'s model-parameter uncertainties are not completely accurate. B. Häussler et al. (2007) stress-tested `GALFIT` and showed that model-parameter uncertainties must be measured explicitly, especially in cases where the parameter space is nonlinear or may have local minima.

For this work, model-parameter uncertainties were determined by a method adapted from §5.2 of A. van der Wel et al. (2012). `GALFIT` was used to simulate images of each sample host galaxy in every filter using the best-fit parameters of their Sérsic components. A point-source was added at ±0.5 mag from its best-fit magnitude in steps of 0.1 mag, as J. M. Gabor et al. (2009) showed that point-source magnitudes are recoverable in this fashion within ±0.5 mag. Noise from empty parts

[28] Specifically, both `DETECT_THRESH` and `ANALYSIS_THRESH` were set to $1.5\sigma$ above the local background. Higher thresholds were tested but resulted in non-detection of any residual structure from the host galaxies.

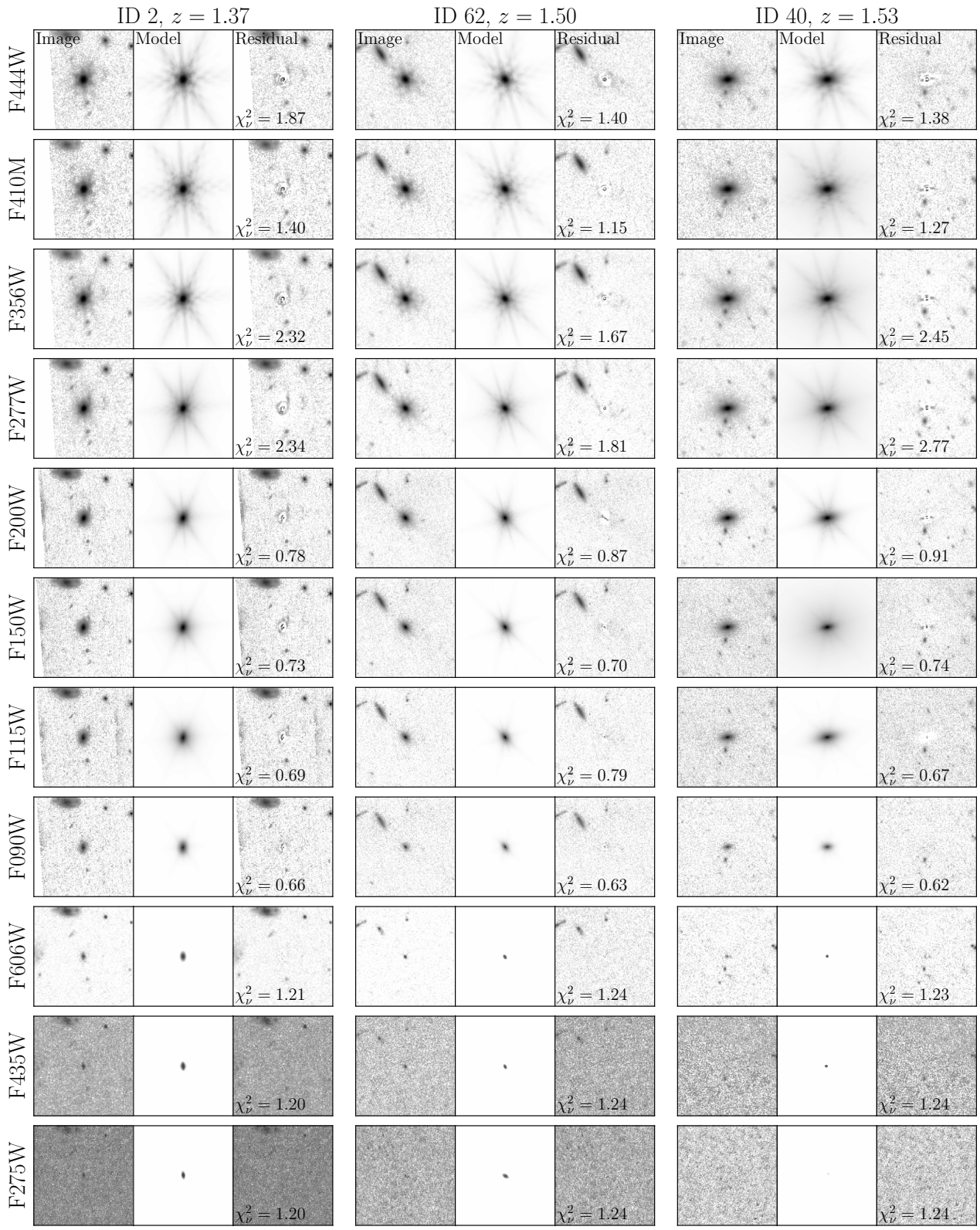



**Figure 2.** Images of the modeling done for IDs 2 (left), 62 (middle), and 40 (right). Each set of 3 images corresponds to the indicated filter; the leftmost image is the galaxy image, the middle image is the best-fit model light profile found by `GALFIT`, and the right image is the residual. The goodness-of-fit statistic $\chi^2_\nu$ of each is shown in the bottom right of the residual panel of each. All images are $\sim 4''$ on a side. Compared to detections in JWST, detections in HST were less frequent.

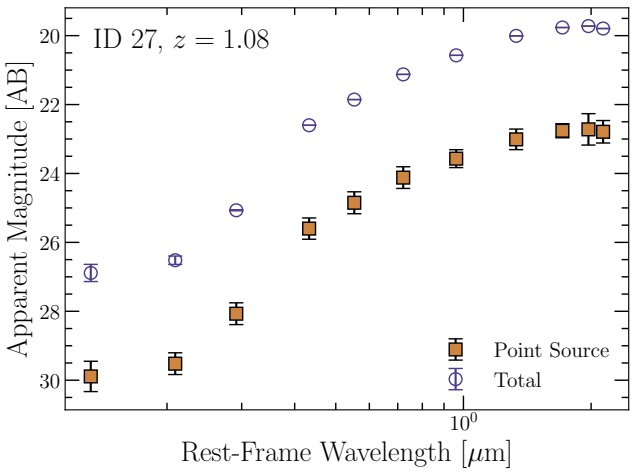



**Figure 3.** The UV–visible–NIR point source magnitude as a function of rest-frame wavelength for ID 27. Point-source magnitudes are drawn in gold with error bars from the procedure of §3.2, and the total magnitudes and error bars from O24 are drawn in blue. Their uncertainties are very small in the NIRCam filters, generally significant only for faint objects in HST filters. The fitting procedure outlined in §3.1 and Appendix A is capable of determining point-source magnitudes down to $\sim 30$ mag, where they are unimportant compared to host-galaxy emission.

of the science mosaics was added to each simulated image, resulting in 11 noisy simulated images, each with a known point-source magnitude. `GALFIT` was run on all simulated images using the same configuration as described in Appendix A, and

$$\Delta m \equiv m' - m \tag{1}$$

was measured for every fitting result using the "recovered" and "true" point-source magnitudes $m'$ and $m$. Then, for every filter, the mean of $\Delta m$ was computed as

$$\langle \Delta m \rangle = \frac{1}{N} \sum_{k=1}^{N} \Delta m_k \tag{2}$$

for the number of convergent simulated image fitting runs $N$. For most objects, this was all 11 runs in each filter with a detection. For the entire sample, the mean and median of $\langle \Delta m \rangle$ were $-0.08$ mag and $-0.06$ mag, respectively, indicating that §3.1's procedure for measuring point-source magnitudes is robust.

The point-source magnitude uncertainty in each filter for each object was computed as the population standard deviation of the distribution of $\Delta m_k$,

$$\delta m_{\rm PS} \equiv \left[ \frac{1}{N} \sum_{k=1}^{N} \left( \Delta m_k - \langle \Delta m \rangle \right)^2 \right]^{1/2} . \tag{3}$$

An example of the point-source measurement results is shown in Figure 3. For most objects, the shape of the point-source magnitudes are consistent with the SED shapes of obscured AGN over the wavelength where power-law-like emission "ramps up" (see, e.g., E. Treister et al. 2004; E. Hatziminaoglou et al. 2009; F. Pozzi et al. 2010; M. Stalevski 2012; M. Stalevski et al. 2016; G. Yang et al. 2023, and the references therein). Because many objects in the O24 catalog are probably obscured AGN, this is expected.

Photometry of the host galaxies was computed using the O24 catalog photometry and the point-source measurements from §3. Host-galaxy flux densities in mJy were computed using

$$S_{\rm host} = \zeta \times \left( 10^{-0.4 m_{\rm cat}} - 10^{-0.4 m_{\rm PS}} \right) , \tag{4}$$

where $\zeta$ is the constant $3.631 \times 10^6$ mJy, $m_{\rm cat}$ is the galaxy-integrated `SourceExtractor` magnitude from O24 and $m_{\rm PS}$ is the point-source magnitude from §3.1. Flux density uncertainties were computed as

$$\delta S_{\rm host} = \zeta' \times \left( 10^{-0.8 m_{\rm cat}} \delta m_{\rm cat}^2 + 10^{-0.8 m_{\rm PS}} \delta m_{\rm PS}^2 \right)^{1/2} \tag{5}$$

for $\delta m_{\rm cat}$ from O24 photometry,[29] $\delta m_{\rm PS}$ from §3.2, and the constant $\zeta' = \ln 10^{0.4\zeta} = 3.344 \times 10^6$ mJy. Generally speaking, point sources were only appreciable, in the sense that the computed host galaxy flux significantly differed from the measured host+AGN flux, in the JWST filters. The catalog flux densities capture irregular, non-axisymmetric features of the galaxies, and the host galaxy flux densities depend on models only insofar as the models determine the galaxies' central magnitudes and thus their point-source magnitudes.

## 4. RESULTS & DISCUSSION

### 4.1. *Host Galaxy SEDs & Parameter Estimation*

We used the energy balance SED-fitting code `CIGALE`[30] (M. Boquien et al. 2019; G. Yang et al. 2020, 2022; D. Burgarella et al. 2025) version 2025.1 to fit SEDs and estimate the physical parameters of the host galaxies. Table 3 describes the `CIGALE` configuration. Five uniquely-seeded stochastic star-formation histories (SFHs)[31] from C. Carvajal-Bohorquez et al. (2025) were

[29] Photometric uncertainties in the O24 photometry are not published, but they are the `SourceExtractor` `MAGERR_AUTO` uncertainties on the published measurements.

[30] https://cigale.lam.fr/

[31] C. Carvajal-Bohorquez et al. (2025) is based on JWST observations of galaxies with $6 \lesssim z \lesssim 12$. However, stochastic star formation is evidenced in, e.g., C. Papovich et al. (2004) and D. Kim et al. (2019) for lower redshifts.

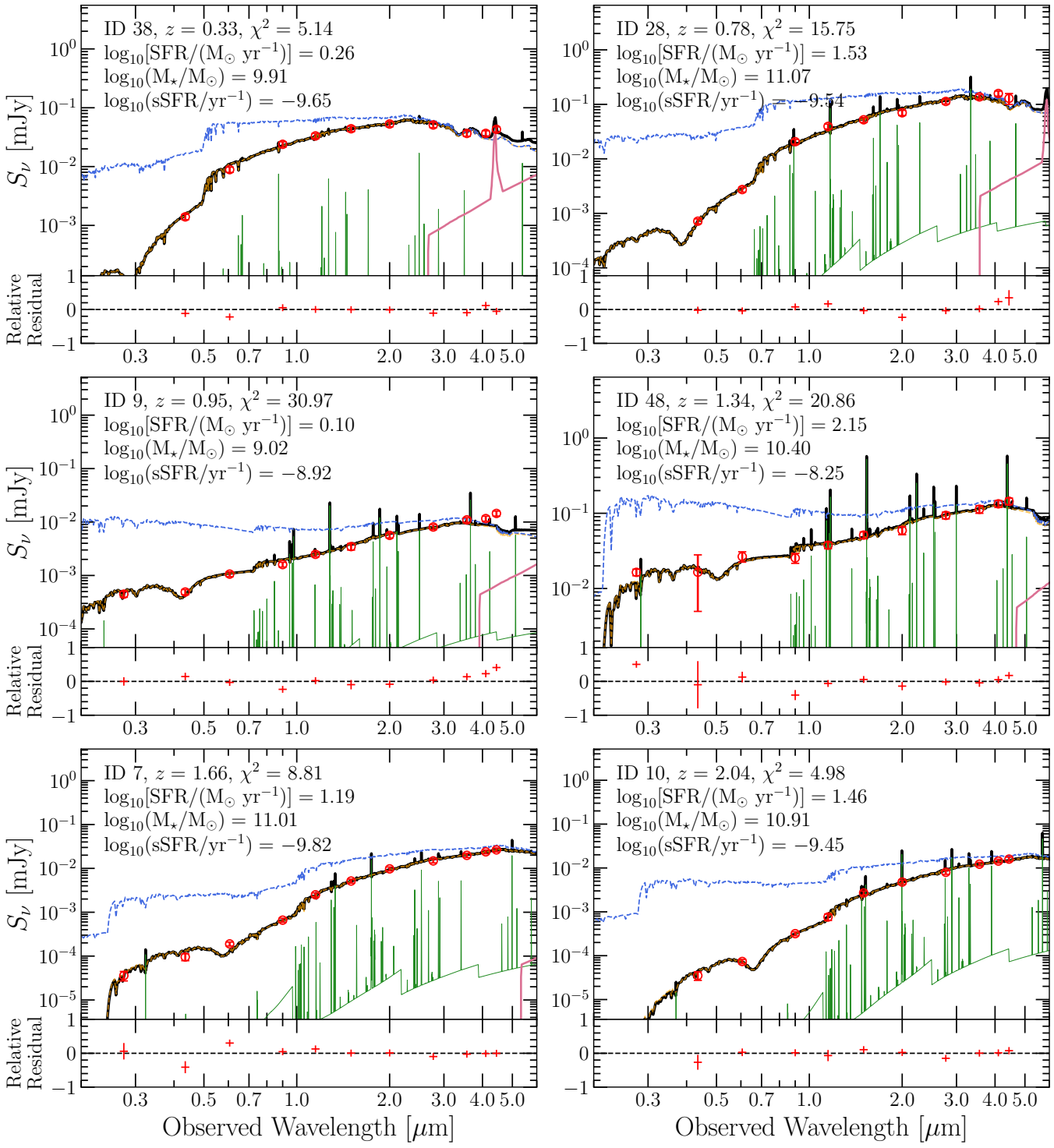



**Figure 4.** Best-fit host-galaxy SEDs from CIGALE. The redshift, $\chi^2$ of the SED fit, and logarithms of the SFR, stellar mass, and sSFR $\equiv$ SFR/M$_\star$ shown in the upper left of each panel. Host-galaxy flux densities are plotted in red with uncertainties computed via Equation (5), and model SEDs are drawn in black. Nebular emission is drawn in green, stellar attenuated and unattenuated are drawn in orange and blue, respectively, and dust emission, if present, is drawn in pink. The objects shown are representative of the redshift range of the sample, $z \sim 0.3$–2 and are ordered by increasing redshift (down and right is higher). All those shown had detections in all 11 filters except for IDs 10/28/38, which are non-detections in HST/F275W.

considered for each object, with a delayed-$\tau$ SFH as a baseline (`sfhstochastic_carvajal2025` module). A G. Bruzual & S. Charlot (2003) simple stellar population with solar metallicity with a G. Chabrier (2003) initial mass function (IMF) was chosen (`bc03` module). Lines were computed according to the `CLOUDY`-based A. K. Inoue (2011) templates, and nebular continua including free-free, free-bound, and two-photon processes were modeled via the `nebular` module. Dust attenuation was modeled using a D. Calzetti et al. (2000) law, modified to account for potential starburst or quenching activity (`dustatt_modified_starburst` module). Because the photometry extends into the NIR, dust emission was accounted for by the D. A. Dale et al. (2014) templates (`dale2014` module) with AGN fraction set to zero. Redshift was not left as a free parameter in fitting; where available, spectroscopically-confirmed redshifts were given to `CIGALE`. Otherwise, the photometric redshifts from the O24 catalog were used. This was done in the `redshifting` module, which also includes intergalactic medium (IGM) transmission from A. Meiksin (2006).

`CIGALE` was configured to add an additional 10% uncertainty to all input flux densities to account for any uncertainties that were not considered or propagated in §3.2. The results found by `CIGALE`'s `bayes` routine were used to infer physical parameters as they are less model-dependent than the best-fit (by SED $\chi^2_\nu$) results.

Even though the SEDs are informed by UV–visible measurements from HST, the 11-band photometric coverage is simply not enough to constrain SFH in detail. However, as delayed-$\tau$ SFHs are generally flexible (see, e.g., A. C. Carnall et al. 2019; J. Leja et al. 2019, and the references therein), and stochastic feedback mechanisms may be at play in AGN–host systems, a stochastic SFH constructed around a baseline delayed-$\tau$ trend is sufficient for the purposes of this study (i.e., it does not restrict the possibility of starburst or quenching behaviors while still following the expected delayed-$\tau$ behavior). Even though the SFH cannot be inferred from the 11-filter photometry alone,[32] a stochastic SFH with a delayed-$\tau$ baseline allows appropriately for the star formation preferred by the data.

The SED fitting results' $\chi^2_\nu$ distribution had median, mean, and standard deviation of 0.90, 1.66, and 2.33, respectively. Example SEDs of objects whose redshifts trace the sample's redshift range are shown in Figure 4. Their shapes are typical of galaxies whose emission is dominated by stellar continuum (e.g., K. G. Iyer et al. 2026, and references therein), which is expected for objects whose AGN emission has been removed.

[32] While the *SFH* is not resolved by the current suite of photometry, the present stellar mass and SFR are well-constrained because of rest-frame UV–visible coverage that observes young stars and rest-frame NIR observations that constrain the older stellar population.

### 4.2. *Host Galaxy Star Formation*

Star formation in the Universe reached its peak at $z \sim 2$ and has been on the decline since (P. Madau & M. Dickinson 2014), but galaxies exhibit a variety of star-forming behaviors at all redshifts. Observations have parameterized dependence on stellar mass and redshift with a canonical star-forming main sequence (SFMS, K. G. Noeske et al. 2007), and galaxies' SFRs are compared by computing offsets,

$$\Delta\mathrm{SFMS} \equiv \log_{10}\left(\mathrm{SFR}/\mathrm{SFR}_{\mathrm{MS}}\right) \tag{6}$$

for main-sequence star-formation rate $\mathrm{SFR}_{\mathrm{MS}}$.

The left panel of Figure 5 shows ΔSFMS from the P. Popesso et al. (2023) SFMS for the NIRCam-selected objects in this study and for X-ray- and radio-selected objects from R. Ortiz et al. (2026, in prep.) and S. P. Willner et al. (2026), respectively. The medians of the radio-selected, NIRCam-selected, and X-ray-selected objects fall at SFMS offsets of −0.06, −0.58, and −1.13 dex, respectively. Remarkably, a part of the NIRCam sample appears to form a "bridge" between the X-ray and radio samples' star-forming properties, which are in line with expectations from, e.g., G. Mountrichas et al. (2022) and B. Zhang et al. (2025). The transition region of the parameter space contains 11/36 galaxies in the sample, suggesting that NIRCam finds a population of AGN whose hosts that are in a transition between quiescent or star-forming stages in their evolution. This further suggests that NIR-bright point sources signal an evolutionary phase when AGN are actively quenching star formation.

Simulations predict that inflows of gas from the pristine reservoirs of the circumgalactic medium (CGM) can trigger nuclear starbursts and rapid growth of the central SMBH (e.g., T. Di Matteo et al. 2005; P. F. Hopkins et al. 2006; A. Dekel & A. Burkert 2014; A. Zolotov et al. 2015). The AGN then grows in a heavily-obscured, IR-bright phase powered by CGM inflows (e.g., P. F. Hopkins & L. Hernquist 2009), which is consistent with the IR-luminous galaxy-quasar evolutionary picture in D. B. Sanders et al. (1988). AGN feedback can subsequently quench host star formation via negative feedback processes, giving rise to a population of galaxies with bright nuclear regions and on their way to quiescence. In this framework, it is possible that dusty NIRCam-selected AGN trace a transitional phase of AGN growth between

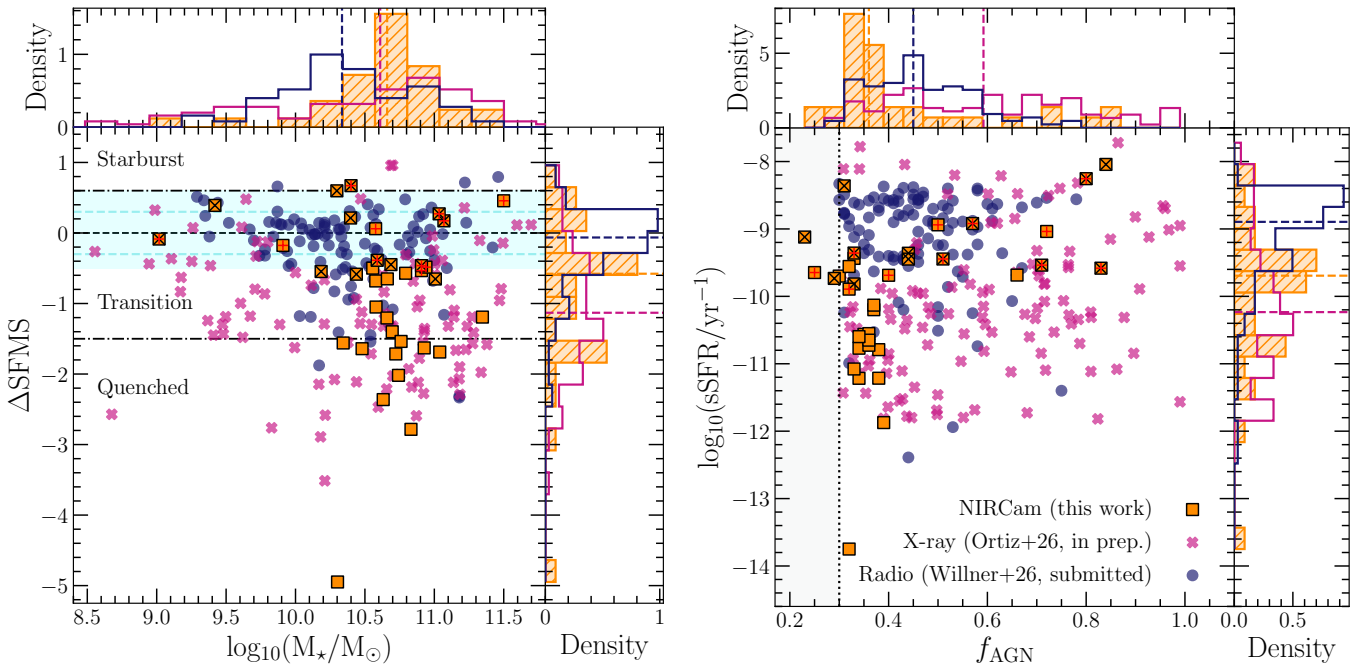



**Figure 5.** Star-forming properties of the sample. This study's NIRCam-selected objects are plotted as orange squares, and the X-ray- (R. Ortiz et al. 2026, in prep.) and radio-selected (S. P. Willner et al. 2026) objects are plotted as pink Xs and blue circles, respectively. NIRCam-selected objects with an X-ray counterpart (W. P. Maksym et al. in prep.) are plotted with a black ×; those with a radio counterpart (M. Hyun et al. 2023) are plotted with a red +. Objects with both X-ray and radio counterparts are plotted with both symbols. The central plots are flanked by two normalized histograms of the quantities that their axes are parallel to. The distribution of each quantity is drawn in its sample's respective color, and the median values are marked with colored dashed lines. *Left panel:* Star-forming main sequence offsets using $\mathrm{SFR_{MS}}$ from P. Popesso et al. (2023) as a function of logarithmic stellar mass. The cyan-shaded region marks the extent of the SFMS with the upper boundary separating it from a starburst region (e.g., G. Rodighiero et al. 2011) and the lower boundary separating it from the transition region between main-sequence and quenched (A. Renzini & Y.-j. Peng 2015). The ±0.3 dex region is bounded by darker dashed cyan lines in the cyan-shaded region. *Right panel:* Logarithmic sSFR as a function of $f_{\mathrm{AGN}}$ (from O24 for the NIRCam sample). A vertical dotted line marks $f_{\mathrm{AGN}} = 0.3$. Three NIRCam-selected objects do not satisfy this cut but have point-source cores (O24, §2.2). The outlying NIRCam-selected object well below the others is ID 30 at $z = 1.58$, a non-detection in HST/F275W.

short-timescale X-ray AGN activity (e.g., K. Schawinski et al. 2015) and longer-lived radio AGN activity (e.g., J. Bird et al. 2008).

The NIRCam-selected objects with X-ray and/or radio counterparts don't fall into the same parts of the parameter space as the X-ray- or radio-selected objects that lack NIRCam point-source morphology. The former are almost entirely contained within ±0.3–0.6 dex of ΔSFMS = 0; there are 10 of these objects, and only 6 within ±0.3 dex of ΔSFMS = 0. Most ordinary galaxies have $|\Delta\mathrm{SFMS}| \leq 0.3$ (e.g., E. Daddi et al. 2007; M. Pannella et al. 2009), but many of these sources do not.

The only starburst object in the NIRCam sample is ID 23 at $z = 1.12$, which has both radio and X-ray counterparts. Its apparent morphology is, from Figure 1, early-type, consistent with its Sérsic indices from GALFIT. It is possible that ID 23 is a compact radio galaxy, similar to objects found by R. A. Windhorst et al. (e.g., 1991, 1992), but the detection of X-ray flux suggests current SMBH accretion activity (e.g., D. M. Alexander & R. C. Hickox 2012; D. M. Alexander et al. 2025), which points to simultaneous AGN activity and star formation. O24 (their Figure 7) found that 10/66 CPGs were starburst, 3 of which were shown to have point-source cores and were thus selected for this study; this fraction is much higher than the single starburst object found in the NIRCam sample (Figure 5 left). The difference does not arise from the different SFMS prescriptions (J. S. Speagle et al. 2014 by O24, P. Popesso et al. 2023 here) because they produce similar results over the redshift range of our sample. Because Figure 5 shows host-galaxy properties with minimal AGN contamination, the O24 SEDs appear to have been biased by rest UV–visible AGN emission. The likely scenario is that a fraction of the total emission in these wavelengths came from an AGN, but CIGALE interpreted it as an excess of flux from young stars, and thus the SFRs were biased

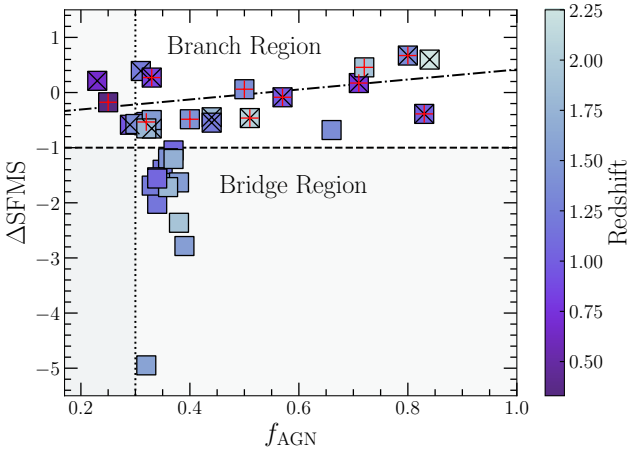



**Figure 6.** Offsets from the SFMS as a function of $f_{AGN}$. For clarity, only the NIRCam-selected sample is shown. X-ray and radio detections are marked with × and +, respectively, and marker colors correspond to redshift as shown in the scale bar. The vertical dotted line is the $f_{AGN} \geq 0.3$ cut used in the sample selection, and the horizontal dashed line at $\Delta SFMS = -1$ is used to separate the bridge portion of the sample from the branch. The branch region at the upper right contains 22 of the 36 sample galaxies. The thick black dash-dotted line is a linear fit to these galaxies with a coefficient of determination $R^2 = 0.17$.

upward (as expected from, e.g., S. Erroz-Ferrer et al. 2013).

Given that galaxies' stellar masses and SFRs are often strongly correlated (e.g., L. Bisigello et al. 2018), it's useful to consider the sSFR. This is done in the right panel of Figure 5 with respect to the $f_{AGN}$ for the samples. The three NIRCam-selected objects with $f_{AGN} \leq 0.3$, selected on the basis of their point-source cores, are either X-ray or radio-detected, suggestive of NIRCam's ability to find *bona fide* AGN by their nuclear point sources in the reddest filters. The median $f_{AGN}$ for the NIRCam-selected objects is 0.35, which is almost certainly an underestimate. Many objects in the O24 catalog have lower SED AGN fractions, indicating that the sample is biased to have a lower $f_{AGN}$.

The sSFRs have similar trends as the SFMS offsets: the median of the NIRCam-selected objects' sSFR is nearly equidistant from those of the X-ray and radio samples, with the X-ray median being lower and the radio median being higher. The NIRCam-selected sources with X-ray and/or radio counterparts are clustered around the radio sample's median sSFR. That the two panels' star-forming patterns are similar suggests that NIRCam's bridge trend is a feature of the data, not just an artifact of the SFMS or the assumptions it makes.

### 4.3. *The Branch and the Bridge*

For objects with X-ray and/or radio counterparts and those wth similar SFMS offsets, there is a positive correlation between ΔSFMS and $f_{AGN}$. As shown in Figure 6, this group is cleanly separated from the rest of the NIRCam-selected sample with a common $\Delta SFMS > -1$: though we do not use it in this study, $\Delta SFMS = -1$ is commonly taken as a quenched threshold (e.g., M. Donnari et al. 2021), and galaxies above it appear to form a "branch" in this parameter space. The NIRCam-selected sample's distribution of the SFMS offsets is mirrored by its sSFR distribution. This correlation has been seen before (e.g., J. Aird et al. 2019), and it suggests that the NIRCam-selected objects' AGN emission is correlated with ongoing star formation in the host. As most of these sources have X-ray counterparts, this may be evidence of positive AGN feedback (e.g., J. Silk 2013) that is presently or very recently occurring but that has not yet pushed the host galaxies into starburst or transition regions. Alternatively, the correlation might suggest simultaneous fueling of both the central SMBH and star formation in the galaxy regardless of feedback.

There is no clear preference of high- or low-$z$ for branch objects, though the highest-redshift object in the sample—ID 14, an apparent quasar with detections in all 11 filters, spectroscopically confirmed to be at $z = 2.25$—is a branch object. From the morphologies visible in Figure 1 and visual inspection of `GALFIT` residuals, branch galaxies commonly have spiral structure, while bridge galaxies do not. This is shown in Figure 7 for a selection of objects with these characteristics. Branch galaxies also have more prominent point-source features, especially in the redder filters of NIRCam, as shown in Figure 8 for JWST/F444W, which suggests that branch galaxies host more luminous AGN than bridge galaxies. Figure 8 also shows that branch galaxies' star-formation rates are higher than those of bridge galaxies with very little overlap, further suggesting that these are two distinct populations differentiated by their star-forming properties but not by their stellar masses.

There are 22 branch galaxies and 14 bridge galaxies, identified in Table 1. The existence of these groups paints the picture of host galaxies that are diverging from the SFMS, likely related to their AGN activity. Those that constitute the bridge between radio and X-ray star-forming behavior have lower $f_{AGN}$ and SFRs. They do not have X-ray or radio detections and are heading towards a quenched state if they have not arrived there already. As none of the bridge galaxies are detected in the X-ray or radio, there are two possibili-

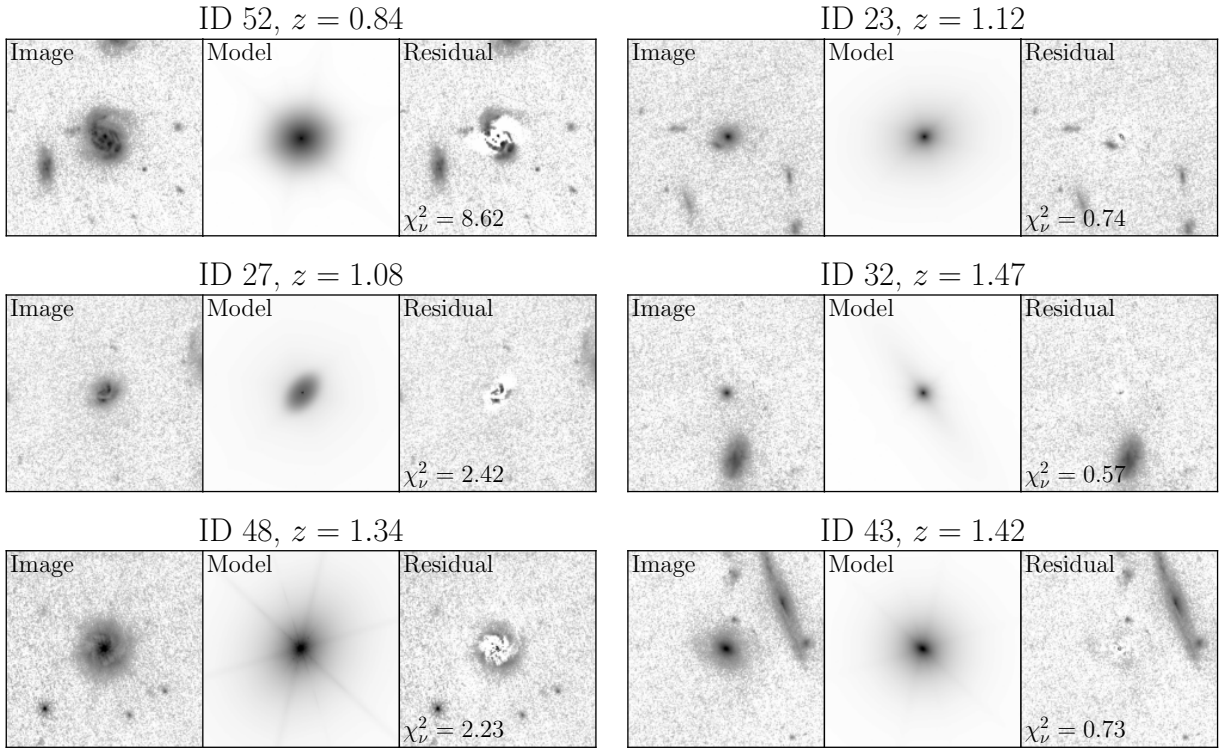



**Figure 7.** JWST/F090W light-profile models for six galaxies. The left column shows branch galaxies and the right column bridge galaxies with IDs and redshifts labeled. For each galaxy, the left panel shows the observed image, the middle panel shows the model, and the right panel shows the residual.

ties. One is that the bridge galaxies are not AGN but are instead galaxies with bright, compact central regions that appear pointlike when convolved with the JWST/NIRCam PSF. The other is that they host low-luminosity or highly obscured AGN. The available data are insufficient to distinguish these possibilities, but if the galaxies do not host AGN, morphological AGN selection with NIRCam is subject to contamination from galaxies that are bright because of compact stellar bulges.

In contrast to the bridge galaxies, galaxies forming the branch in Figure 6 have the brightest point sources in the sample and tend to have X-ray and radio counterparts and therefore likely do host AGN. These galaxies may be currently or very recently experiencing bursts or quenching of star formation in response to AGN feedback, as they are mostly still within ±0.6 dex of the SFMS but further away than the expected ±0.3 dex for genuine main-sequence galaxies. Longer-wavelength observations of NIRCam-selected objects will make the presence or absence of AGN clearer, especially if the AGN are obscured, and can help fully quantify NIRCam's ability to sample a complete AGN population.

## 5. SUMMARY & FUTURE WORK

The sensitivity and angular resolution of JWST/NIRCam allows not only for the morphological selection of AGN candidates but also enables direct studies of the underlying host galaxies. Morphological analysis with NIRCam can identify bright central emission, often coming from luminous AGN activity. NIRCam-selected AGN candidates comprise two distinct groups, best understood in the context of their host-galaxy SFR relative to the SFMS.

- Host galaxies of NIRCam-selected AGN without X-ray and/or radio counterparts form a "bridge" between the higher SFRs of radio-selected objects and the lower SFRs of X-ray-selected objects. The bridge galaxies largely have early-type morphologies with compact, bright cores that show point-source features. These objects are either quenched or in the transition region between star-forming and quenched. The bridge population represents either a non-AGN population with bright, compact stellar bulges, or they are low-luminosity or obscured AGN residing in quenched or actively quenching systems.

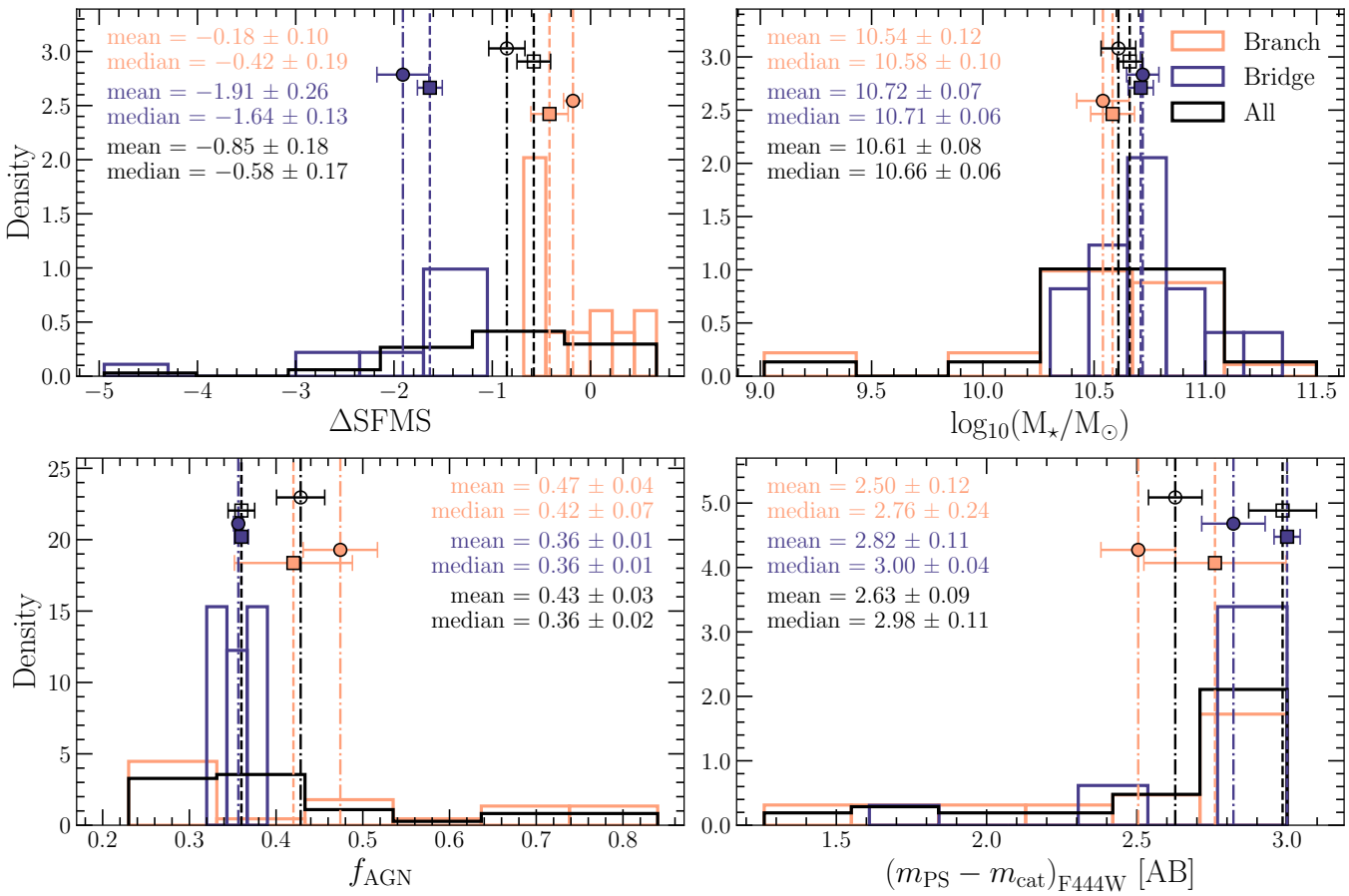



**Figure 8.** Normalized distributions of the NIRCam sample's properties. The *upper left* panel shows SMFS offsets, the *upper right* stellar mass, the *lower left* O24 $f_{\rm AGN}$, and the *lower right* JWST/F444W point-source fraction. The latter is the F444W point-source magnitude $m_{\rm PS}$ (§3.1) minus total magnitude $m_{\rm cat}$ (O24). The bridge distributions are drawn in blue and the branch distributions in orange. The means (circles) and medians (squares) are drawn in dot-dashed and dashed lines in the corresponding colors, and the error bars are the standard errors on the mean and median. Summary statistics are shown in each plot, where the text color corresponds the distribution.

- Host galaxies with X-ray- and/or radio counterparts mostly have SFRs between ±0.3 dex and ±0.6 dex from the SFMS. Their SFMS offsets are positively correlated with $f_{\rm AGN}$. These objects are separate from the bridge and are instead part of a "branch" of galaxies that may have current or recent bursts or quenching of star formation. The AGN are likely impacting the star-forming activity of their hosts and are suggestive of a phase where AGN coexist with galaxies nearby but not on the SFMS. This population is morphologically diverse but includes galaxies with clumpy or spiral structures.

The star-forming behaviors of the bridge and branch populations have no correlation with redshift or stellar mass. Branch galaxies have both brighter and more dominant point sources between the two groups and are definite AGN hosts by the detections of their X-ray and/or radio counterparts. Bridge galaxies may or may not be AGN hosts as they do not have X-ray or radio counterparts.

Future studies similar to this one will offer further insights into whether or not the host galaxies of NIRCam-selected AGN are indeed SFMS-divergent in the sense of §4.2. This sample contains 36 objects from a single catalog, but the methods developed in this study are applicable to any number of objects, and so large-scale analyses of NIRCam-selected host galaxies are possible.

The results of this study suggest rich coevolution between AGN and their host galaxies. However, as this work is concerned expressly with host galaxies' star-forming properties, it is unable to draw conclusions regarding, e.g., SMBH properties or gas kinematics. Results of these kinds are obtainable from studies using codes such as `AGNfitter` (G. Calistro Rivera et al. 2016; L. N. Martínez-Ramírez et al. 2024) or `GELATO` (R. E. Hviding et al. 2022) that are designed to dis-

tinguish AGN and host galaxy emission. Spectroscopic studies of NIRCam-selected objects will be particularly illuminating on this front and will be useful in identifying the presence and type(s) of feedback mechanisms suggested by this study's results (e.g., quenching).

Most critically, high-resolution observations of these objects and other similar sources, especially in the mid-infrared, will offer additional constraints on host-galaxy properties not well-determined by just UV–visible–NIR photometry (J. Lyu et al. 2024). With just these wavelengths, objects' SFHs could not be resolved in any meaningful way, and so ages of the most recent starbursts, etc. cannot be identified from SED fitting. In this case, conclusions can be drawn because X-ray and radio detections provided insight into the timescales of AGN activity, but the timescales of change in the hosts' SFR could not be quantified directly. Mid-infrared observations at high resolution with, e.g, JWST's Mid-Infrared Instrument (MIRI) would both provide invaluable constraints on the SFH and allow dust attenuation and other host properties properties to be inferred from SEDs with less degeneracy. In addition, it is ambiguous whether or not the bridge galaxies are genuinely AGN hosts: it is possible that they are hosts to highly obscured AGN that are actively quenching star formation, but the NIR does not offer insight here. Mid-infrared observations will be pivotal in determining if bridge galaxies do host this type of AGN, or if morphological AGN selection is contaminated by centrally-bright, non-AGN objects. Given its resolution in its wavelength range, JWST/MIRI is the only suitable tool to advance host galaxy studies like this one, and its observations will address what NIRCam cannot. Nonetheless, this work presents NIRCam imaging as a prime tool for identifying and analyzing AGN populations.

## ACKNOWLEDGMENTS

This work is based on observations associated with programs JWST-GTO-2738 and 1176 made with the NASA/ESA/CSA James Webb Space Telescope (JWST) and observations associated with programs HST-GO-15278, 16252 and 16793 made with the NASA/ESA Hubble Space Telescope (HST). The JWST and HST data were obtained from the Mikulski Archive for Space Telescopes at the Space Telescope Science Institute (STScI), which is operated by the Association of Universities for Research in Astronomy, Inc. (AURA), under NASA contracts NAS 5-03127 (JWST) and NAS 5-26555 (HST). This work uses data obtained at the MMT Observatory, a facility jointly operated by the University of Arizona and the Smithsonian Institution. RAW, SHC, and RAJ acknowledge support from NASA JWST Interdisciplinary Scientist grants NAG5-12460, NNX14AN10G and 80NSSC18K0200 from GSFC. RAJ, RO, RAW, SHC, AMK, BLF and CNAW acknowledge support from HST grants HST-GO-15278.*, 16252.* and 16793.* from STScI, which is operated by AURA under contract NAS 5-26555 from NASA. CNAW acknowledges funding from the JWST/NIRCam contract NASS-0215 to the University of Arizona. Work by CJC acknowledges support from the European Research Council (ERC) Advanced Investigator Grant EPOCHS (788113). BLF thanks the Berkeley Center for Theoretical Physics for their hospitality during the writing of this paper. This work is sponsored (in part) by the Chinese Academy of Sciences (CAS) through a grant to the CAS South America Center for Astronomy. C.C. acknowledges NSFC grant No. 11803044 and 12173045. This work is supported by the China Manned Space Program with grant no. CMS-CSST-2025-A07. C.C. is supported by Chinese Academy of Sciences South America Center for Astronomy (CASSACA) Key Research Project E52H540301.

We also acknowledge the indigenous peoples of Arizona, including the Akimel O'odham (Pima) and Pee Posh (Maricopa) Indian Communities, whose care and keeping of the land has enabled us to be at ASU's Tempe campus in the Salt River Valley, where much of our work was conducted.

All the JWST and HST data used in this paper can be found in MAST: 10.17909/yans-cz11.

*Software:* `Astropy` ( Astropy Collaboration et al. 2013, 2018, 2022), `IDL` Astronomy Library (W. B. Landsman 1993), `SourceExtractor` (E. Bertin & S. Arnouts 1996), `GALFIT` (C. Y. Peng et al. 2002, 2010), `CIGALE` (M. Boquien et al. 2019; G. Yang et al. 2020, 2022; D. Burgarella et al. 2025), `STPSF` (M. D. Perrin et al. 2014), `Trilogy` (D. Coe et al. 2012)

*Facilities:* James Webb Space Telescope, Hubble Space Telescope, MMT Observatory, Chandra X-Ray Observatory, Karl G. Jansky Very Large Array, Mikulski Archive for Space Telescopes

## REFERENCES

Aird, J., Coil, A. L., & Georgakakis, A. 2019, MNRAS, 484, 4360, doi: 10.1093/mnras/stz125

Alexander, D. M., & Hickox, R. C. 2012, NewAR, 56, 93, doi: 10.1016/j.newar.2011.11.003

Alexander, D. M., Bauer, F. E., Brandt, W. N., et al. 2003, AJ, 126, 539, doi: 10.1086/376473
Alexander, D. M., Hickox, R. C., Aird, J., et al. 2025, NewAR, 101, 101733, doi: 10.1016/j.newar.2025.101733
Assef, R. J., Stern, D., Kochanek, C. S., et al. 2013, ApJ, 772, 26, doi: 10.1088/0004-637X/772/1/26
Astropy Collaboration, Robitaille, T. P., Tollerud, E. J., et al. 2013, A&A, 558, A33, doi: 10.1051/0004-6361/201322068
Astropy Collaboration, Price-Whelan, A. M., Sipőcz, B. M., et al. 2018, AJ, 156, 123, doi: 10.3847/1538-3881/aabc4f
Astropy Collaboration, Price-Whelan, A. M., Lim, P. L., et al. 2022, ApJ, 935, 167, doi: 10.3847/1538-4357/ac7c74
Bertin, E. 2013, PSFEx: Point Spread Function Extractor,, Astrophysics Source Code Library, record ascl:1301.001 http://ascl.net/1301.001
Bertin, E., & Arnouts, S. 1996, A&AS, 117, 393, doi: 10.1051/aas:1996164
Bird, J., Martini, P., & Kaiser, C. 2008, ApJ, 676, 147, doi: 10.1086/527534
Bisigello, L., Caputi, K. I., Grogin, N., & Koekemoer, A. 2018, A&A, 609, A82, doi: 10.1051/0004-6361/201731399
Blank, M., & Duschl, W. J. 2012, in Journal of Physics Conference Series, Vol. 372, Journal of Physics Conference Series (IOP), 012053, doi: 10.1088/1742-6596/372/1/012053
Blanton, M. R., Hogg, D. W., Bahcall, N. A., et al. 2003, ApJ, 594, 186, doi: 10.1086/375528
Bonaventura, N., Rieke, G. H., Lyu, J., et al. 2026, ApJ, 997, 47, doi: 10.3847/1538-4357/ae1ef8
Boquien, M., Burgarella, D., Roehlly, Y., et al. 2019, A&A, 622, A103, doi: 10.1051/0004-6361/201834156
Bradley, L., Sipőcz, B., Robitaille, T., et al. 2025, astropy/photutils: 2.3.0, 2.3.0 Zenodo, doi: 10.5281/zenodo.17129028
Bruzual, G., & Charlot, S. 2003, MNRAS, 344, 1000, doi: 10.1046/j.1365-8711.2003.06897.x
Burbidge, G. 1970, Comments on Astrophysics and Space Physics, 2, 144
Burgarella, D., Buat, V., Theulé, P., et al. 2025, A&A, 699, A336, doi: 10.1051/0004-6361/202554231
Calistro Rivera, G., Lusso, E., Hennawi, J. F., & Hogg, D. W. 2016, ApJ, 833, 98, doi: 10.3847/1538-4357/833/1/98
Calzetti, D., Armus, L., Bohlin, R. C., et al. 2000, ApJ, 533, 682, doi: 10.1086/308692
Caon, N., Capaccioli, M., & D'Onofrio, M. 1993, MNRAS, 265, 1013, doi: 10.1093/mnras/265.4.1013
Cardelli, J. A., Clayton, G. C., & Mathis, J. S. 1989, ApJ, 345, 245, doi: 10.1086/167900
Carnall, A. C., Leja, J., Johnson, B. D., et al. 2019, ApJ, 873, 44, doi: 10.3847/1538-4357/ab04a2
Carvajal-Bohorquez, C., Ciesla, L., Laporte, N., et al. 2025, A&A, 704, A290, doi: 10.1051/0004-6361/202556471
Casertano, S., de Mello, D., Dickinson, M., et al. 2000, AJ, 120, 2747, doi: 10.1086/316851
Chabrier, G. 2003, PASP, 115, 763, doi: 10.1086/376392
Ciesla, L., Charmandaris, V., Georgakakis, A., et al. 2015, A&A, 576, A10, doi: 10.1051/0004-6361/201425252
Ciotti, L., & Bertin, G. 1999, A&A, 352, 447, doi: 10.48550/arXiv.astro-ph/9911078
Coe, D., Umetsu, K., Zitrin, A., et al. 2012, ApJ, 757, 22, doi: 10.1088/0004-637X/757/1/22
Daddi, E., Dickinson, M., Morrison, G., et al. 2007, ApJ, 670, 156, doi: 10.1086/521818
Dale, D. A., Helou, G., Magdis, G. E., et al. 2014, ApJ, 784, 83, doi: 10.1088/0004-637X/784/1/83
de Vaucouleurs, G. 1948, Annales d'Astrophysique, 11, 247
Dekel, A., & Burkert, A. 2014, MNRAS, 438, 1870, doi: 10.1093/mnras/stt2331
Dewsnap, C., Barmby, P., & Gallagher, S. C. 2025, PASP, 137, 114101, doi: 10.1088/1538-3873/ae1662
Dey, A., Schlegel, D. J., Lang, D., et al. 2019, AJ, 157, 168, doi: 10.3847/1538-3881/ab089d
Di Matteo, T., Springel, V., & Hernquist, L. 2005, Nature, 433, 604, doi: 10.1038/nature03335
Donley, J. L., Koekemoer, A. M., Brusa, M., et al. 2012, ApJ, 748, 142, doi: 10.1088/0004-637X/748/2/142
Donnari, M., Pillepich, A., Nelson, D., et al. 2021, MNRAS, 506, 4760, doi: 10.1093/mnras/stab1950
Driver, S. P., Hill, D. T., Kelvin, L. S., et al. 2011, MNRAS, 413, 971, doi: 10.1111/j.1365-2966.2010.18188.x
Duncan, K. J., Windhorst, R. A., Koekemoer, A. M., et al. 2023, MNRAS, 522, 4548, doi: 10.1093/mnras/stad1267
Dunlop, J. S., McLure, R. J., Kukula, M. J., et al. 2003, MNRAS, 340, 1095, doi: 10.1046/j.1365-8711.2003.06333.x
Elvis, M., Maccacaro, T., Wilson, A. S., et al. 1978, MNRAS, 183, 129, doi: 10.1093/mnras/183.2.129
Erroz-Ferrer, S., Knapen, J. H., Mohd Noh Velastín, E. A. N., Ryon, J. E., & Hagen, L. M. Z. 2013, MNRAS, 436, 3135, doi: 10.1093/mnras/stt1797
Fabian, A. C. 1999, MNRAS, 308, L39, doi: 10.1046/j.1365-8711.1999.03017.x
Fabian, A. C. 2012, ARA&A, 50, 455, doi: 10.1146/annurev-astro-081811-125521
Fanaroff, B. L., & Riley, J. M. 1974, MNRAS, 167, 31P, doi: 10.1093/mnras/167.1.31P
Farrah, D., Afonso, J., Efstathiou, A., et al. 2003, MNRAS, 343, 585, doi: 10.1046/j.1365-8711.2003.06696.x

Fazio, G. G., Hora, J. L., Allen, L. E., et al. 2004, ApJS, 154, 10, doi: 10.1086/422843
Gabor, J. M., Impey, C. D., Jahnke, K., et al. 2009, ApJ, 691, 705, doi: 10.1088/0004-637X/691/1/705
Gardner, J. P., Mather, J. C., Abbott, R., et al. 2023, PASP, 135, 068001, doi: 10.1088/1538-3873/acd1b5
Gezari, S., Martin, D. C., Forster, K., et al. 2013, ApJ, 766, 60, doi: 10.1088/0004-637X/766/1/60
Giacconi, R., Rosati, P., Tozzi, P., et al. 2001, ApJ, 551, 624, doi: 10.1086/320222
Hatziminaoglou, E., Fritz, J., & Jarrett, T. H. 2009, MNRAS, 399, 1206, doi: 10.1111/j.1365-2966.2009.15390.x
Häussler, B., McIntosh, D. H., Barden, M., et al. 2007, ApJS, 172, 615, doi: 10.1086/518836
Hazard, C., Mackey, M. B., & Shimmins, A. J. 1963, Nature, 197, 1037, doi: 10.1038/1971037a0
Heckman, T. M. 1980, A&A, 87, 152
Hopkins, P. F., & Hernquist, L. 2009, ApJ, 698, 1550, doi: 10.1088/0004-637X/698/2/1550
Hopkins, P. F., Hernquist, L., Cox, T. J., et al. 2006, ApJS, 163, 1, doi: 10.1086/499298
Hviding, R. E., Hainline, K. N., Rieke, M., et al. 2022, AJ, 163, 224, doi: 10.3847/1538-3881/ac5e33
Hyun, M., Im, M., Smail, I. R., et al. 2023, ApJS, 264, 19, doi: 10.3847/1538-4365/ac9bf4
Inoue, A. K. 2011, MNRAS, 415, 2920, doi: 10.1111/j.1365-2966.2011.18906.x
Iyer, K. G., Pacifici, C., Calistro-Rivera, G., & Lovell, C. C. 2026, in Encyclopedia of Astrophysics, Vol. 4, 236–281, doi: 10.1016/B978-0-443-21439-4.00127-9
Jansen, R. A., & Windhorst, R. A. 2018, PASP, 130, 124001, doi: 10.1088/1538-3873/aae476
Joseph, P., Sreekumar, P., Stalin, C. S., et al. 2022, MNRAS, 516, 2300, doi: 10.1093/mnras/stac2388
Kauffmann, G., Heckman, T. M., Tremonti, C., et al. 2003, MNRAS, 346, 1055, doi: 10.1111/j.1365-2966.2003.07154.x
Kewley, L. J., Groves, B., Kauffmann, G., & Heckman, T. 2006, MNRAS, 372, 961, doi: 10.1111/j.1365-2966.2006.10859.x
Khachikian, E. Y., & Weedman, D. W. 1974, ApJ, 192, 581, doi: 10.1086/153093
Kim, D., Jansen, R. A., Windhorst, R. A., Cohen, S. H., & McCabe, T. J. 2019, ApJ, 884, 21, doi: 10.3847/1538-4357/ab385c
Kirkpatrick, A., Urry, C. M., Brewster, J., et al. 2020, ApJ, 900, 5, doi: 10.3847/1538-4357/aba358
Kocevski, D. D., Barro, G., McGrath, E. J., et al. 2023, ApJL, 946, L14, doi: 10.3847/2041-8213/acad00
Kormendy, J., & Richstone, D. 1995, ARA&A, 33, 581, doi: 10.1146/annurev.aa.33.090195.003053
Kotilainen, J. K., Ward, M. J., Boisson, C., et al. 1992a, MNRAS, 256, 125, doi: 10.1093/mnras/256.1.125
Kotilainen, J. K., Ward, M. J., Boisson, C., Depoy, D. L., & Smith, M. G. 1992b, MNRAS, 256, 149, doi: 10.1093/mnras/256.1.149
Krist, J. 1993, in Astronomical Society of the Pacific Conference Series, Vol. 52, Astronomical Data Analysis Software and Systems II, ed. R. J. Hanisch, R. J. V. Brissenden, & J. Barnes, 536
Krist, J. E., Hook, R. N., & Stoehr, F. 2011, in Society of Photo-Optical Instrumentation Engineers (SPIE) Conference Series, Vol. 8127, Optical Modeling and Performance Predictions V, ed. M. A. Kahan, 81270J, doi: 10.1117/12.892762
Lacy, M., Storrie-Lombardi, L. J., Sajina, A., et al. 2004, ApJS, 154, 166, doi: 10.1086/422816
Laha, S., Reynolds, C. S., Reeves, J., et al. 2021, Nature Astronomy, 5, 13, doi: 10.1038/s41550-020-01255-2
Landsman, W. B. 1993, in Astronomical Society of the Pacific Conference Series, Vol. 52, Astronomical Data Analysis Software and Systems II, ed. R. J. Hanisch, R. J. V. Brissenden, & J. Barnes, 246
Latif, M. A., Aftab, A., & Whalen, D. J. 2024, AJ, 167, 251, doi: 10.3847/1538-3881/ad3b97
Leja, J., Carnall, A. C., Johnson, B. D., Conroy, C., & Speagle, J. S. 2019, ApJ, 876, 3, doi: 10.3847/1538-4357/ab133c
Lyu, J., Alberts, S., Rieke, G. H., et al. 2024, ApJ, 966, 229, doi: 10.3847/1538-4357/ad3643
Madau, P., & Dickinson, M. 2014, ARA&A, 52, 415, doi: 10.1146/annurev-astro-081811-125615
Magorrian, J., Tremaine, S., Richstone, D., et al. 1998, AJ, 115, 2285, doi: 10.1086/300353
Martin, D. C., Fanson, J., Schiminovich, D., et al. 2005, ApJL, 619, L1, doi: 10.1086/426387
Martínez-Ramírez, L. N., Calistro Rivera, G., Lusso, E., et al. 2024, A&A, 688, A46, doi: 10.1051/0004-6361/202449329
Meiksin, A. 2006, MNRAS, 365, 807, doi: 10.1111/j.1365-2966.2005.09756.x
Miyazaki, S., Komiyama, Y., Kawanomoto, S., et al. 2018, PASJ, 70, S1, doi: 10.1093/pasj/psx063
Mountrichas, G., Masoura, V. A., Xilouris, E. M., et al. 2022, A&A, 661, A108, doi: 10.1051/0004-6361/202142792
Nayakshin, S. 2014, MNRAS, 437, 2404, doi: 10.1093/mnras/stt2059

Noeske, K. G., Weiner, B. J., Faber, S. M., et al. 2007, ApJL, 660, L43, doi: 10.1086/517926
O'Brien, R., Jansen, R. A., Grogin, N. A., et al. 2024, ApJS, 272, 19, doi: 10.3847/1538-4365/ad3948
Oke, J. B., & Gunn, J. E. 1983, ApJ, 266, 713, doi: 10.1086/160817
Ortiz, R., Windhorst, R. A., Cohen, S. H., et al. 2024, ApJ, 974, 258, doi: 10.3847/1538-4357/ad6d5e
Pannella, M., Carilli, C. L., Daddi, E., et al. 2009, ApJL, 698, L116, doi: 10.1088/0004-637X/698/2/L116
Papovich, C., Dickinson, M., Ferguson, H. C., et al. 2004, ApJL, 600, L111, doi: 10.1086/381075
Patel, S. G., Holden, B. P., Kelson, D. D., et al. 2012, ApJL, 748, L27, doi: 10.1088/2041-8205/748/2/L27
Peng, C. Y., Ho, L. C., Impey, C. D., & Rix, H.-W. 2002, AJ, 124, 266, doi: 10.1086/340952
Peng, C. Y., Ho, L. C., Impey, C. D., & Rix, H.-W. 2010, AJ, 139, 2097, doi: 10.1088/0004-6256/139/6/2097
Perrin, M. D., Sivaramakrishnan, A., Lajoie, C.-P., et al. 2014, in Society of Photo-Optical Instrumentation Engineers (SPIE) Conference Series, Vol. 9143, Space Telescopes and Instrumentation 2014: Optical, Infrared, and Millimeter Wave, ed. J. M. Oschmann, Jr., M. Clampin, G. G. Fazio, & H. A. MacEwen, 91433X, doi: 10.1117/12.2056689
Planck Collaboration, Ade, P. A. R., Aghanim, N., et al. 2016, A&A, 594, A13, doi: 10.1051/0004-6361/201525830
Planck Collaboration, Aghanim, N., Akrami, Y., et al. 2020, A&A, 641, A6, doi: 10.1051/0004-6361/201833910
Popesso, P., Concas, A., Cresci, G., et al. 2023, MNRAS, 519, 1526, doi: 10.1093/mnras/stac3214
Pozzi, F., Vignali, C., Comastri, A., et al. 2010, A&A, 517, A11, doi: 10.1051/0004-6361/200913043
Ramírez, E. A., Tadhunter, C. N., Dicken, D., et al. 2014, MNRAS, 439, 1270, doi: 10.1093/mnras/stt2444
Renzini, A., & Peng, Y.-j. 2015, ApJL, 801, L29, doi: 10.1088/2041-8205/801/2/L29
Richstone, D., Ajhar, E. A., Bender, R., et al. 1998, Nature, 385, A14, doi: 10.48550/arXiv.astro-ph/9810378
Rieke, G. H., Sun, Y., Lyu, J., et al. 2025, ApJ, 994, 35, doi: 10.3847/1538-4357/adff79
Rieke, M. J., Kelly, D. M., Misselt, K., et al. 2023, PASP, 135, 028001, doi: 10.1088/1538-3873/acac53
Roberts-Borsani, G., Treu, T., Mason, C., et al. 2021, ApJ, 910, 86, doi: 10.3847/1538-4357/abe45b
Rodighiero, G., Daddi, E., Baronchelli, I., et al. 2011, ApJL, 739, L40, doi: 10.1088/2041-8205/739/2/L40
Saikia, P., Wrzosek, R., Gelfand, J., et al. 2025, ApJ, 989, 29, doi: 10.3847/1538-4357/ade709
Sajina, A., Lacy, M., & Scott, D. 2005, ApJ, 621, 256, doi: 10.1086/426536
Sanders, D. B., Soifer, B. T., Elias, J. H., et al. 1988, ApJ, 325, 74, doi: 10.1086/165983
Schawinski, K., Koss, M., Berney, S., & Sartori, L. F. 2015, MNRAS, 451, 2517, doi: 10.1093/mnras/stv1136
Schlafly, E. F., Meisner, A. M., & Green, G. M. 2019, ApJS, 240, 30, doi: 10.3847/1538-4365/aafbea
Schmidt, M. 1963, Nature, 197, 1040, doi: 10.1038/1971040a0
Sérsic, J. L. 1963, Boletin de la Asociacion Argentina de Astronomia La Plata Argentina, 6, 41
Sérsic, J. L. 1968, Atlas de Galaxias Australes
Seyfert, C. K. 1943, ApJ, 97, 28, doi: 10.1086/144488
Silk, J. 2013, ApJ, 772, 112, doi: 10.1088/0004-637X/772/2/112
Silk, J., & Rees, M. J. 1998, A&A, 331, L1, doi: 10.48550/arXiv.astro-ph/9801013
Silver, R., Civano, F., Zhao, X., et al. 2026, ApJ, 998, 200, doi: 10.3847/1538-4357/ae328e
Simard, L., Mendel, J. T., Patton, D. R., Ellison, S. L., & McConnachie, A. W. 2011, ApJS, 196, 11, doi: 10.1088/0067-0049/196/1/11
Speagle, J. S., Steinhardt, C. L., Capak, P. L., & Silverman, J. D. 2014, ApJS, 214, 15, doi: 10.1088/0067-0049/214/2/15
Stalevski, M. 2012, Bulgarian Astronomical Journal, 18, 3
Stalevski, M., Ricci, C., Ueda, Y., et al. 2016, MNRAS, 458, 2288, doi: 10.1093/mnras/stw444
Stern, D., Eisenhardt, P., Gorjian, V., et al. 2005, ApJ, 631, 163, doi: 10.1086/432523
Stern, D., Assef, R. J., Benford, D. J., et al. 2012, ApJ, 753, 30, doi: 10.1088/0004-637X/753/1/30
Sturm, E., González-Alfonso, E., Veilleux, S., et al. 2011, ApJL, 733, L16, doi: 10.1088/2041-8205/733/1/L16
Tran, H. D. 1995a, ApJ, 440, 565, doi: 10.1086/175296
Tran, H. D. 1995b, ApJ, 440, 578, doi: 10.1086/175297
Tran, H. D. 1995c, ApJ, 440, 597, doi: 10.1086/175298
Treister, E., Urry, C. M., Chatzichristou, E., et al. 2004, ApJ, 616, 123, doi: 10.1086/424891
van Breugel, W., Fragile, C., Anninos, P., & Murray, S. 2004, in IAU Symposium, Vol. 217, Recycling Intergalactic and Interstellar Matter, ed. P.-A. Duc, J. Braine, & E. Brinks, 472, doi: 10.48550/arXiv.astro-ph/0312282
van der Wel, A., Bell, E. F., Häussler, B., et al. 2012, ApJS, 203, 24, doi: 10.1088/0067-0049/203/2/24
Wang, L., De Lucia, G., Fontanot, F., & Hirschmann, M. 2019, MNRAS, 482, 4454, doi: 10.1093/mnras/sty2998

Whitaker, K. E., Kriek, M., van Dokkum, P. G., et al. 2012, ApJ, 745, 179, doi: 10.1088/0004-637X/745/2/179

Willmer, C. N. A., Ly, C., Kikuta, S., et al. 2023, ApJS, 269, 21, doi: 10.3847/1538-4365/acf57d

Willner, S. P., Gim, H. B., Polletta, M. d. C., et al. 2023, ApJ, 958, 176, doi: 10.3847/1538-4357/acfdfb

Willner, S. P., Gim, H. B., Polletta, M. d. C., et al. 2026, ApJ, submitted

Windhorst, R. A., Mathis, D. F., & Keel, W. C. 1992, ApJL, 400, L1, doi: 10.1086/186634

Windhorst, R. A., Burstein, D., Mathis, D. F., et al. 1991, ApJ, 380, 362, doi: 10.1086/170596

Windhorst, R. A., Cohen, S. H., Hathi, N. P., et al. 2011, ApJS, 193, 27, doi: 10.1088/0067-0049/193/2/27

Windhorst, R. A., Cohen, S. H., Jansen, R. A., et al. 2023, AJ, 165, 13, doi: 10.3847/1538-3881/aca163

Yang, G., Boquien, M., Buat, V., et al. 2020, MNRAS, 491, 740, doi: 10.1093/mnras/stz3001

Yang, G., Boquien, M., Brandt, W. N., et al. 2022, ApJ, 927, 192, doi: 10.3847/1538-4357/ac4971

Yang, G., Caputi, K. I., Papovich, C., et al. 2023, ApJL, 950, L5, doi: 10.3847/2041-8213/acd639

York, D. G., Adelman, J., Anderson, Jr., J. E., et al. 2000, AJ, 120, 1579, doi: 10.1086/301513

Zakamska, N. L., Strauss, M. A., Krolik, J. H., et al. 2006, AJ, 132, 1496, doi: 10.1086/506986

Zhang, B., Zou, F., Brandt, W. N., et al. 2025, ApJ, 978, 9, doi: 10.3847/1538-4357/ad9278

Zhao, X., Civano, F., Willmer, C. N. A., et al. 2024, ApJ, 965, 188, doi: 10.3847/1538-4357/ad2b61

Zhuang, M.-Y., Ho, L. C., & Shangguan, J. 2021, ApJ, 906, 38, doi: 10.3847/1538-4357/abc94d

Zhuang, M.-Y., & Shen, Y. 2024, ApJ, 962, 139, doi: 10.3847/1538-4357/ad1183

Zinn, P.-C., Middelberg, E., Norris, R. P., & Dettmar, R.-J. 2013, ApJ, 774, 66, doi: 10.1088/0004-637X/774/1/66

Zolotov, A., Dekel, A., Mandelker, N., et al. 2015, MNRAS, 450, 2327, doi: 10.1093/mnras/stv740

# APPENDIX

**Table 1**. NIRCam-Selected AGN-Host Candidates

| ID | Right Ascension | Declination | Spoke | $z$ | Core Type | $f_{\rm AGN}$ | Bridge/Branch | X-Ray ID | Radio ID |
|---|---|---|---|---|---|---|---|---|---|
| (1) | (2) | (3) | (4) | (5) | (6) | (7) | (8) | (9) | (10) |
| 2 | 260.756207 | 65.713177 | 1b | 1.37 | P | 0.50 | Branch | — | 314 |
| 6 | 260.701250 | 65.776180 | 1ab | 1.00 | P | 0.83 | Branch | 451 | 232 |
| 7 | 260.697887 | 65.777933 | 1ab | 1.66 | P | 0.33 | Branch | 452 | — |
| 9 | 260.695583 | 65.784352 | 1b | 0.95 | P | 0.57 | Branch | 453 | 223 |
| 10 | 260.746297 | 65.784221 | 1b | 2.04 | P | 0.51 | Branch | 102 | 300 |
| 11 | 260.719022 | 65.786260 | 1b | 1.17 | U | 0.35 | Bridge | — | — |
| 13 | 260.641043 | 65.787557 | 4 | 1.16 | U | 0.34 | Bridge | — | — |
| 14 | 260.536970 | 65.795297 | 4 | 2.2508 | P | 0.84 | Branch | 119 | — |
| 23 | 260.456228 | 65.807676 | 4 | 1.12 | B | 0.34 | Bridge | — | — |
| 24 | 260.524706 | 65.809982 | 4 | 1.20 | B | 0.33 | Bridge | — | — |
| 25 | 260.483404 | 65.811818 | 4 | 1.20 | P | 0.31 | Branch | 463 | — |
| 27 | 260.531751 | 65.815627 | 4 | 1.08 | B | 0.32 | Branch | — | 63 |
| 28 | 260.896667 | 65.817463 | 2 | 0.7791 | P | 0.71 | Branch | 106 | 497 |
| 30 | 260.814880 | 65.821168 | 2 | 1.58 | P | 0.32 | Bridge | — | — |
| 32 | 260.898138 | 65.821819 | 2 | 1.47 | U | 0.36 | Bridge | — | — |
| 33 | 260.423208 | 65.823911 | 4 | 1.07 | B | 0.37 | Bridge | — | — |
| 34 | 260.768573 | 65.826200 | 2 | 1.51 | U | 0.38 | Bridge | — | — |
| 35 | 260.538451 | 65.827557 | 4 | 0.9442 | P | 0.29 | Branch | 155 | — |
| 38 | 260.919468 | 65.831341 | 2 | 0.33 | P | 0.25 | Branch | — | 528 |
| 39 | 260.965050 | 65.834642 | 2 | 0.6726 | P | 0.23 | Branch | 126 | — |
| 40 | 260.661331 | 65.832686 | 3 | 1.53 | U | 0.39 | Bridge | — | — |
| 42 | 260.498867 | 65.833758 | 4 | 1.8016 | P | 0.44 | Branch | 162 | — |
| 43 | 260.661990 | 65.841400 | 3 | 1.42 | B | 0.36 | Bridge | — | — |
| 48 | 260.639560 | 65.844960 | 3 | 1.3369 | B | 0.80 | Branch | 109 | 142 |
| 52 | 260.624274 | 65.867878 | 3 | 0.84 | B | 0.33 | Branch | 165 | 121 |
| 53 | 260.681038 | 65.869282 | 3 | 1.88 | B | 0.72 | Branch | — | 207 |
| 55 | 260.738030 | 65.902876 | 3 | 1.36 | P | 0.66 | Branch | — | — |
| 56 | 260.708784 | 65.876954 | 3 | 1.79 | U | 0.36 | Bridge | — | — |
| 57 | 260.651265 | 65.893590 | 3 | 1.05 | U | 0.34 | Bridge | — | — |
| 58 | 260.668029 | 65.877818 | 3 | 1.43 | B | 0.40 | Branch | — | 187 |
| 59 | 260.665718 | 65.877257 | 3 | 1.91 | B | 0.38 | Bridge | — | — |
| 60 | 260.690274 | 65.899640 | 3 | 1.37 | U | 0.30 | Branch | — | — |
| 62 | 260.709682 | 65.880570 | 3 | 1.50 | U | 0.33 | Branch | — | — |
| 63 | 260.629030 | 65.874101 | 3 | 1.77 | U | 0.32 | Branch | — | — |
| 64 | 260.649498 | 65.870951 | 3 | 1.20 | P | 0.44 | Branch | 132 | — |

**Table 1** *continued*

**Table 1** *(continued)*

| ID | Right Ascension | Declination | Spoke | $z$ | Core Type | $f_{\rm AGN}$ | Bridge/Branch | X-Ray ID | Radio ID |
|---|---|---|---|---|---|---|---|---|---|
| (1) | (2) | (3) | (4) | (5) | (6) | (7) | (8) | (9) | (10) |
| 66 | 260.672783 | 65.911116 | 3 | 1.70 | P | 0.37 | Bridge | — | — |

NOTE—Column descriptions are as follows: (1) ID from O24; (2,3) ICRS positions in decimal degrees from O24; (4) spoke of the JWST NEP-TDF containing the object; (5) redshift, where spectoscopically-confirmed redshifts are listed to 4 decimal places and O24 photometric redshifts are listed to 2 decimal places; (6) JWST/F444W core type from O24 (B = bulge, P = point source, U = undetermined); (7) AGN fraction from $0.1 - 30.0$ $\mu$m from O24; bridge ($\Delta$SFMS $< -1$) or branch ($\Delta$SFMS $> -1$) classification; (9) X-ray counterpart ID from W. P. Maksym et al. (in prep.); (10) radio counterpart ID from M. Hyun et al. (2023).

**Table 2**. Table of GALFIT Output Parameters for JWST Filters

| ID | Filter | Disk mag | Disk $r_e$ | Disk $n$ | Bulge mag | Bulge $r_e$ | Bulge $n$ | $m_{\rm PS}$ | $\delta m_{\rm PS}$ | $\chi^2_\nu$ |
|---|---|---|---|---|---|---|---|---|---|---|
| | | mag | pix | | mag | pix | | mag | mag | |
| (1) | (2) | (3) | (4) | (5) | (6) | (7) | (8) | (9) | (10) | (11) |
| **2** | F444W | 20.46 | 4.00 | 1.92 | 23.19 | 0.79 | 3.00 | 23.35 | 0.20 | 1.87 |
| | F410M | 20.96 | 4.00 | 1.31 | 21.52 | 3.84 | 4.29 | 23.46 | 0.32 | 1.41 |
| | F356W | 20.72 | 4.00 | 1.93 | 23.72 | 0.00 | 3.00 | 23.72 | 0.15 | 2.32 |
| | F277W | 21.12 | 4.00 | 1.36 | 22.38 | 13.19 | 3.00 | 23.92 | 0.31 | 2.34 |
| | F200W | 21.53 | 5.72 | 1.20 | 24.44 | 25.50 | 3.00 | 24.44 | 0.31 | 0.78 |
| | F150W | 22.26 | 6.26 | 0.78 | 22.52 | 6.58 | 3.00 | 24.61 | 0.31 | 0.73 |
| | F115W | 22.97 | 7.52 | 0.58 | 22.84 | 8.27 | 3.00 | 25.16 | 1.14 | 0.69 |
| | F090W | 23.26 | 6.31 | 0.99 | 26.11 | 0.00 | 3.00 | 26.11 | 0.31 | 0.66 |
| **6** | F444W | 19.97 | 4.00 | 1.55 | 22.91 | 10.84 | 3.00 | 22.91 | 0.30 | 4.89 |
| | F410M | 20.29 | 4.99 | 1.63 | 21.77 | 1.08 | 3.00 | 22.44 | 0.40 | 2.99 |
| | F356W | 20.35 | 5.29 | 1.44 | 19.47 | 37664.35 | 9.09 | 22.47 | 0.27 | 6.59 |
| | F277W | 20.63 | 6.09 | 1.23 | 20.52 | 7648.14 | 5.61 | 23.52 | 0.30 | 5.14 |
| | F200W | 21.36 | 7.66 | 0.97 | 23.26 | 2.71 | 3.00 | 24.14 | 0.89 | 1.34 |
| | F150W | 22.30 | 9.19 | 0.48 | 22.24 | 7.09 | 3.00 | 24.52 | 0.90 | 1.41 |
| | F115W | 22.09 | 7.75 | 1.01 | 25.02 | 0.00 | 3.00 | 25.02 | 0.29 | 1.35 |
| | F090W | 23.20 | 7.94 | 0.51 | 23.00 | 66.10 | 3.00 | 25.79 | 0.28 | 1.00 |
| ... | ... | ... | ... | ... | ... | ... | ... | ... | ... | ... |

NOTE—The full Table 2 is available as a machine-readable table (MRT). Column descriptions are as follows: (1) ID from O24; (2) JWST filter; (3) magnitude of disk Sérsic; (4) half-light radius of the disk Sérsic; (5) Sérsic index of the disk Sérsic; (6) magnitude of the bulge Sérsic; (7) half-light radius of the bulge Sérsic; (8) Sérsic index of the bulge Sérsic; (9) magnitude of the point-source; (10) uncertainty in the magnitude of the point-source; (11) $\chi^2_\nu$ of the GALFIT model. Each ID (bolded) has 8 associated rows, one for each JWST filter. Pixel $r_e$ values listed as 0.00 denote fits for which the $r_e$ was much less than 1 pixel — see the end of Appendix A for discussion of Sérsic component radii. The measurement of the uncertainty in the point-source magnitude is not done by GALFIT and is detailed in §3.2.

**Table 3**. CIGALE Configuration for SED Fitting

| Model Component | SED Module | Parameter | Details |
|---|---|---|---|
| Star-formation history | sfhstochastic_carvajal2025 | $\tau_{\rm main}$ [a] | 0.1, 0.5, 1.0, 2.0 Gyr |
| | | $\rm age_{oldest}$ [b] | 0.1, 0.5, 1, 2, 2.5, 3.0 Gyr |
| | | $\alpha_{\rm PSD}$ [c] | 1.5, 2.0, 2.5 |
| | | $\tau_{\rm break}$ [d] | 0.1, 0.15, 0.2 Gyr |
| | | $\sigma_{\rm SFH}$ [e] | 0.2, 0.4, 0.6 |
| | | Number of SFH seeds [f] | 5 |
| Stellar populations | bc03 | IMF | G. Chabrier (2003) |
| | | $Z_\star$ [g] | 0.02 |
| | | $\rm age_{separation}$ [h] | 0.01, 0.05, 0.1 Gyr |
| Nebular emission | nebular | $\log_{10} U$ [i] | −2.0 |
| | | $Z_{\rm gas}$ [j] | 0.02 |
| | | $n_{\rm e^-}$ [k] | 100 $\rm cm^{-3}$ |
| | | $f_{\rm escape}$ [l] | 0.0 |
| | | $f_{\rm dust}$ [m] | 0.0 |
| | | lines_width | 300 $\rm km\ s^{-1}$ |
| Dust attenuation | dustatt_modified_starburst | $E(B-V)_{\rm lines}$ [n] | 0.1, 0.3, 0.5, 0.7, 1.0, 2.0 |
| | | $E(B-V)_{\rm factor}$ [o] | 0.44 |
| | | uv_bump_wavelength [p] | 217.5 nm |
| | | uv_bump_width [q] | 35.0 nm |
| | | uv_bump_amplitude [r] | 3.0 (Milky Way) |
| | | $\delta_{\rm attenuation}$ [s] | -0.5, -0.25, 0.0 |
| | | Ext_law_emission_lines [t] | Milky Way |
| | | $R_V = A_V/E(B-V)$ [u] | 3.1 (Milky Way) |
| Dust emission | dale2014 | AGN fraction [v] | 0.0 |
| | | $\alpha_{\rm dust}$ [w] | 1.5, 2.0, 2.5 |
| Redshift & IGM | redshifting | Source redshift $z$ | spec-$z$, else O24 photo-$z$ [x] |

NOTE—CIGALE fitting was done using 17,321,040 models, with 524,880 per redshift. The precision on ages and timescales is ±1 Myr. [a]$e$-folding time of the main stellar population, [b]age of the oldest stars in the galaxy, [c]slope of the power spectrum density (damped random walk), [d]decorrelation timescale, [e]dex amplitude of long-term SFH variability, [f]number of seeds for each SFH model computed, each of which corresponding to a unique SFH (see D. Burgarella et al. 2025), [g]stellar populations' metallicity, [h]age of the separation between young and old stellar populations, [i]logarithm of the ionization parameter, [j]gas metallicity, [k]electron ($e^-$) number density, [l]fraction of Lyman continuum photons escaping the galaxy, [m]fraction of Lyman continuum photons absorbed by dust, [n]color excess of nebular lines, [o]reduction factor on $E(B-V)_{\rm lines}$ when computing stellar continuum attenuation, [p]central wavelength of UV bump, [q]FWHM of UV bump, [r]amplitude of UV bump, [s]power-law slope modifying the D. Calzetti et al. (2000) attenuation curve, [t]extinction law for computing emission line fluxes; the Milky Way extinction law was modeled as done in J. A. Cardelli et al. (1989), [u]ratio of V-band dust extinction to $E(B-V)$, also from J. A. Cardelli et al. (1989), [v]fractional AGN contribution to AGN emission, set to zero for this study; note that this is not the SED fractional AGN contribution $f_{\rm AGN}$ in O24, [w]power-law slope of dust mass distribution with respect to radiation field heating intensities (see Equation (1) of D. A. Dale et al. 2014), [x]see §2.1; we used spectroscopic redshifts if available and O24 photometric redshifts otherwise.

## A. TECHNICAL GALFIT CONFIGURATION

GALFIT was provided with 266 × 266 pixel (∼8″ × 8″) galaxy images and masks of nearby objects derived from SourceExtractor (E. Bertin & S. Arnouts 1996) segmentation maps. For fitting in the JWST filters, GALFIT was given stamps from pipeline-generated error (ERR) images as sigma images. For fitting in the HST filters, GALFIT was allowed to compute internal sigma images because no global error images were produced in the HST data reduction. Weight (WHT) images were produced in the HST data reduction, but due to image pixel noise correlation (see, e.g., the Appendix of S. Casertano et al. 2000) and the non-uniform depth of the science images (see R. O'Brien et al. 2024, their Figure 1), the naive ERR = $1/\sqrt{\text{WHT}}$ prescription fails to produce acceptable error images. Preliminary fitting attempts using ERR images computed this way almost never converged. All fitting of HST data was done using models with an additional sky component to ensure robust background RMS estimation, where initial sky-background estimates were taken from the global background RMS computed by SourceExtractor before generating a catalog. The sensitivity of GALFIT's best-fit parameters to the sigma image is weak, but the sigma image must be of acceptable quality for GALFIT to compute accurate $\chi^2_\nu$. GALFIT was provided with PSF models, which are discussed in Appendix B.

All models included Sérsic components. The Sérsic profile is treated by GALFIT as a surface-brightness profile parametrized by radial coordinate $r$ and Sérsic index $n > 0$ as

$$\Sigma(r) = \Sigma_e \exp\left\{-\kappa_n\left[\left(\frac{r}{r_e}\right)^{1/n} - 1\right]\right\} \tag{A1}$$

for half-light radius $r_e$ and $\Sigma_e \equiv \Sigma(r = r_e)$. The number $\kappa_n$ is computed so that, for a given $n$, $r_e$ is indeed the half-light radius.[33] The G. de Vaucouleurs (1948) and exponential "disk" profiles are recovered by Equation (A1) for $n = 4$ and $n = 1$, respectively, and the formula's versatility for virtually any $n$ has set a precedent of fitting galaxies with Sérsic profiles (see e.g., J. L. Sérsic 1968; M. R. Blanton et al. 2003; S. P. Driver et al. 2011; L. Simard et al. 2011, and the references within). While Equation (A1) describes a radially symmetric distribution, Sérsic components in the light-profile models were permitted to be elliptical, handled internally by GALFIT.

**Table 4.** GALFIT Constraints for Light Profile Modeling

| Singular Constraints | | Relational Constraints | | |
|---|---|---|---|---|
| Component | Constraint | Component 1 | Component 2 | Constraint |
| Disk Sérsic | ±3 SourceExtractor mag | Disk Sérsic | Bulge Sérsic | Center, ratio |
| Bulge Sérsic | ±3 SourceExtractor mag | Disk Sérsic | point source | Center, ratio |
| point source | ±3 SourceExtractor mag | Disk Sérsic | Bulge Sérsic | Position angle, ratio |
| Disk Sérsic | $0.2 \leq n \leq 2.0$ | Disk Sérsic | point source | ±3 mag |
| Bulge Sérsic | $3.0 \leq n \leq 10.0$ | Bulge Sérsic | point source | ±3 mag |
| Disk Sérsic | $r_e \geq 4$ pix $= 0.''12$ | — | — | — |

NOTE—Constraints with ±3 mag enforce that components are within 3 magnitudes, not necessarily that components are separated by 3 magnitudes. The ratio constraint is a hard constraint that fixes components' parameters by the ratios of their initial values.

This study used one Sérsic component (the "disk Sérsic") to model the extended component of a galaxy and a point source to model unresolved emission from AGN. A second Sérsic component (the "bulge Sérsic") was used to model any compact, central bulge-like feature whose light may contaminate measurements of the point source. GALFIT constraints, listed in Table 4, were chosen to encourage convergence on physically sensible solutions; e.g., components were required to share a common center to avoid "latching onto" small-scale (but resolved), non-axisymmetric features (e.g., clumps), and all model components were restricted to be within ±3 magnitudes of galaxies' measured magnitude to

[33] See L. Ciotti & G. Bertin (1999) for further discussion. Equation (3) of N. Caon et al. (1993) is the equivalent of Equation (A1) in terms of intensities.

avoid too-bright or too-faint components "dragging" the whole fit into non-convergence or an absurd result. Relational constraints on the Sérsic components were imposed so that they remain distinct (i.e., not two disk-like components overlapping each other or two bulge-like components with no disk).

Initial fitting parameters were derived filter-wise for each object from `SourceExtractor` catalogs run in dual-image mode. For JWST filters, the photometry from O24 with JWST/F444W as the detection image was used. New photometry was measured in the HST filters following §2.2 of O24 but with HST/F606W as the detection image to avoid apertures "latching onto" the JWST/F444W PSF's "wings" from a point source that are not present in HST images. For the Sérsic components, the initial position angle and axis ratio were set to the `SourceExtractor` `THETA_IMAGE` and the ratio of the `SourceExtractor` `B_IMAGE` to `A_IMAGE`. The initial half-light radius was estimated with $r_e = \mathrm{FWHM}/3$. The initial Sérsic indices of the "disk" and "bulge" components profiles were set to $n = 1$ and $n = 5$, respectively. All initial point-source magnitudes were set to the `SourceExtractor` catalog's `MAG_AUTO` for that filter. `GALFIT` was allowed to iterate up to 100 times before either converging or being forced to stop.

The Sérsic components' $r_e$ were left unconstrained in fitting except that they were required to be non-zero. This was done so that `GALFIT` was allowed to fit a larger or smaller extended galaxy with the "bulge" Sérsic component if the data preferred an $n$ in the "bulge" range of Table 4 and vice versa. The result of this was that the "bulge" Sérsic was allowed to converge on a larger $r_e$ than the "disk component". The bulge Sérsics were occasionally found to be very small or very large. This is not problematic *for the purposes of measuring a point-source magnitude* because the integrated magnitudes in these cases are not extreme, in the sense that they are not excessively bright or faint. For these reasons, the `GALFIT` results in Table 2 are not true bulge-disk decomposition results but are suitable for subtracting the galaxy's central flux and measuring a point-source magnitude.

## B. POINT-SPREAD-FUNCTION MODELS

High-quality PSF models are the most important part of modeling any point source in `GALFIT`. For JWST fitting, simulated PSF models from `STPSF` (formerly `WebbPSF`, M. D. Perrin et al. 2014) were used for each object's position angle in the JWST NEP-TDF, as determined by its spoke. Two objects in the sample have multiple position angles due to being observed in multiple overlapping "spokes" of the field. In these cases, the PSF models at the appropriate position angles were median-combined, and the results were used as the PSF models given to `GALFIT`. Images of the hybrid PSF models are shown in Figure 9.

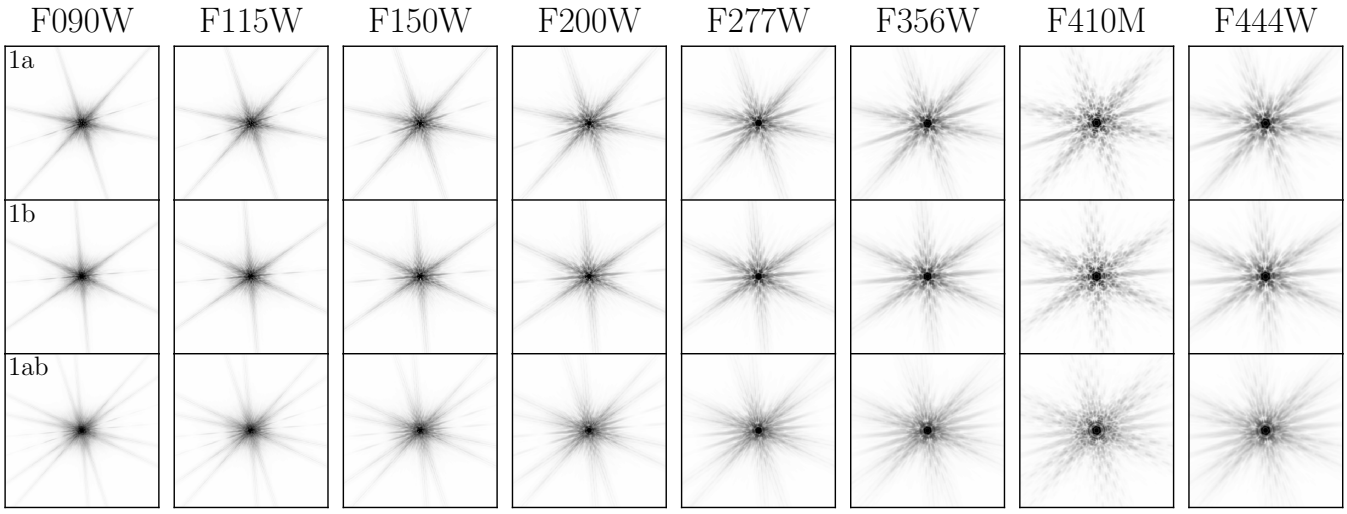



**Figure 9.** Renders of the PSF models given to `GALFIT` for spoke 1's various position angles. The position angle indicators a, b, and ab are as in Table 1. Each row shows a unique position angle, and each column shows a specific filter. These are the `OVERSAMP` extensions of the `STPSF` outputs, matched to the data's pixel scale so that `GALFIT`'s PSF fine sampling is 1.

Unlike the JWST mosaics, the HST mosaics have a large number of position angles drizzled onto the same pixel grid (see Figure 1 of R. O'Brien et al. 2024), which prevents simulation or construction (in the sense of co-adding bright, isolated, high-S/N stars) of PSF images with "wings" aligned with the sample galaxies' position angles. Galactic

stars in the NEP-TDF have low areal density, and the multiplicity of overlapping position angles means that PSF models from stacked high S/N stars are not "well-behaved" in the sense of, e.g., M.-Y. Zhuang & Y. Shen (2024) or C. Dewsnap et al. (2025), and so they cannot be used to construct PSF models for AGN-host decomposition. This was tested explicitly using both `PSFEx` (E. Bertin 2013) and `Photutils`'s `EPSFBuilder` (L. Bradley et al. 2025), which failed to produce results of acceptable quality. Simulation of HST PSFs to median-combine as done for JWST was not feasible either, because the standard HST PSF simulation software `TinyTim` (J. Krist 1993; J. E. Krist et al. 2011) is no longer officially supported by STScI, as HST's instruments have aged and legacy models no longer reproduce their performance.

Because the majority of the HST PSF's light is concentrated in its center, not the wings, a Gaussian HST PSF model was assumed with

$$\sigma_{\rm PSF} = \frac{\rm FWHM}{2\sqrt{2\ln 2}} \tag{B2}$$

for the PSF full width at half maximum (FWHM). We used the PSF FWHMs listed in Table 2 of R. A. Windhorst et al. (2011), which are corrected to account for instrument-specific pixel sampling and telescope optics corrections. The HST PSF models provided to `GALFIT` were drawn directly onto a pixel grid with standard deviations $\sigma_{\rm PSF}$ following Equation (B2) after converting to units of pixels via the $0\farcs030$ pixel$^{-1}$ scale.